Faculty of Physics and Astronomy
Ruprecht-Karls-University Heidelberg

MASTER THESIS

in Physics

submitted by

Sebastian Hähnle

born in Munich

2015

Thermodynamic Properties of Holmium in Gold

The master thesis has been carried out by Sebastian Hähnle
at the Kirchhoff-Institute of Physics
under the supervision of
Prof. Dr. Christian Enss

In this thesis, the thermodynamic properties of holmium in gold were investigated to determine their impact on the performance of metallic magnetic calorimeters. This research was carried out in the context of the ECHo (Electron Capture in ^{163}Ho) experiment, which is designed to investigate the electron neutrino mass in the sub-eV range by means of high precision and high statistics measurement of the ^{163}Ho electron capture spectrum. For this measurement, the ^{163}Ho is implanted directly into the gold absorber of a metallic magnetic calorimeter.
A theoretical model for the thermodynamic properties of holmium in gold was derived, taking into account the crystal field effect and hyperfine interaction of the magnetic moments of single, non-interacting Ho^{3+}-ions, which have a total angular momentum of $J = 8$ and a nuclear spin of $I = 7/2$. The crystal field parameters of Au:Ho were determined to be $W = -0.112$ and $x = -0.357$ using magnetisation measurements on a Au:Ho alloy with 1 % holmium concentration.
The heat capacity of a metallic magnetic calorimeter implanted with about $9{\times}10^{13}$ ^{165}Ho -ions was determined at temperatures between 60 mK and 100 mK, by the analysis of signal amplitudes. No direct evidence of an additional heat capacity is found. However, a deviation from the expected pulse shape can be observed. A possible model describing these results is presented and discussed.

Thermodynamische Eigenschaften von Holmium in Gold

In der vorliegenden Arbeit wurden die thermodynamischen Eigenschaften von Holmium in Gold untersucht, um deren Einfluss auf das Verhalten von metallischen magnetischen Kalorimetern zu bestimmen. Diese Untersuchung erfolgte im Rahmen des ECHo (Electron Capture in ^{163}Ho) Experiments, bei dem das Zerfallsspektrum von ^{163}Ho vermessen wird mit dem Ziel die Neutrinomasse mit hoher Sensitivität zu bestimmen. Hierzu wird ^{163}Ho direkt in metallische magnetische Kalorimeter implantiert.
Ein theoretisches Modell für die thermodynamischen Eigenschaften von Holmium in Gold wurde unter Berücksichtigung des Kristallfelds und der Hyperfeininteraktion der magnetischen Momente von einzelnen, nicht wechselwirkenden Ho^{3+}-Ionen entwickelt. Anhand einer Magnetisierungsmessung an einer Au:Ho Legierung mit 1 % Holmium-Konzentration wurden die Kristallfeldparameter von Au:Ho zu $W = -0.112$ und $x = -0.357$ bestimmt.
Die Wärmekapazität eines metallischen magnetischen Kalorimeters mit 9×10^{13} implantierten ^{165}Ho Ionen wurde im Temperaturbereich von 60 mK bis 100 mK anhand einer Pulshöhenmessung bestimmt und mit vorhergehenden Messungen ohne implantiertem Holmium verglichen. Es wurde keine signifikante Änderung der Wärmekapazität gemessen, allerdings wurden Abweichung von der erwarteten Pulsform beobachtet. Ein mögliches Modell zur Beschreibung dieser Ergebnisse wird vorgeschlagen und diskutiert.

Contents

1. Introduction

The measurement of the neutrino mass is one of the great challenges in modern physics. Originally described as weakly interacting, massless particles in the standard model of particle physics, it took more than 40 years from their first experimental observation until the discovery of neutrino oscillations in 1998 [Fuk98] showed that neutrinos must indeed be massive particles.

Until now, the mass of the three active neutrinos has not been successfully determined and only upper limits have been found [Oli14]. The most precise limit to date has been determined for the electron anti-neutrino mass as $m(\bar{\nu}_e) < 2\,\mathrm{eV}$ by the Mainz/Troitsk experiments, which analysed the β-decay spectrum of ^{3}H [Ber12].

The currently most promising experiments are based on the analysis of the end-point region of low energy β-decay of ^{3}H and electron capture spectra of ^{163}Ho, where the finite mass of the neutrino has the largest effect on the spectral shape. However, only a fraction of $\leq 10^{-12}$ of events lie in the region of interest for these experiments. It is therefore highly important to have a precise understanding of the spectrum and any possible systematic effects in both detector and source.

In the case of experiments based on the analysis of the ^{163}Ho electron capture spectrum, it is of paramount importance that the source is embedded in the detector, in a way that only the energy taken away by the emitted electron neutrino is not measured. The resulting spectrum will then be the complementary spectrum of the emitted neutrino.

In the Electron Capture in ^{163}Ho (ECHo) experiment [Gas14], the enclosure of the source in the detector is achieved by implanting the ^{163}Ho ions directly in the absorber of low temperature metallic magnetic calorimeters. The implantation area will then be covered by a second layer of the absorber material to ensure the full containment of the energy emitted in the electron capture process. Presently, the absorber material used in metallic magnetic calorimeters developed at the Kirchhoff Institute for Physics is gold.

In order to optimize the detector performance, it is important to understand the thermodynamic properties related to the implanted holmium ions. Detailed models describing such systems and the inclusion of electronic bands, will also allow for the study of higher order effects on the de-excitation spectrum of the daughter atom ^{163}Dy.

In this thesis, a theory for the thermodynamic properties of holmium in gold is

derived for the limit of dilute alloys. This theory takes into account the effects of the crystal field and the hyperfine interaction on the magnetic moments of Ho^{3+}-ions in a gold matrix and without mutual interaction. The developed theoretical model will first be applied to the investigation of the specific heat of holmium ions in a gold matrix. A precise understanding of this quantity will allow for the determination of the maximum number of ^{163}Ho which can be implanted in a single detector, so that the additional heat capacity is still smaller than the one of a pure absorber.

For this investigation, three MMC chips, each consisting of 4 pixels, have been implanted with natural holmium ^{165}Ho. The number of ions implanted into the chips were 9×10^{11}, 9×10^{12} and 9×10^{13}, corresponding to ^{163}Ho-activities of 4 Bq, 40 Bq and 400 Bq. The heat capacity of these detectors will then be analysed using the theoretical model obtained in this thesis in addition to the well described heat capacity of a regular MMC. In this thesis a full characterisation of the detector with 9×10^{13} implanted holmium ions was carried out.

In Chapter 2, the different approaches used for experiments designed for the determination of the electron (anti-)neutrino mass are introduced. In particular the investigation of the electron capture of ^{163}Ho in the ECHo experiment is described. An overview of the experimental challenges in ECHo is given, motivating the need for a precise understanding of the thermodynamic properties of Au:Ho dilute alloys.

Chapter 3 describes the principles of the detector type used in the ECHo experiment, metallic magnetic calorimeters. In particular, the design of the detectors used in this thesis is presented.

The theory for the thermodynamic properties of holmium ions in gold is given in chapter 4. Solutions for magnetisation and heat capacity are obtained using numerical calculations, which take into account the crystal field effect, hyperfine interaction and external magnetic field. The crystal field parameters of Au:Ho are obtained by the analysis of magnetisation measurements on a Au:Ho alloy with 1 % holmium concentration.

The required elements for the heat capacity measurement at low temperatures are described in chapter 5, introducing the cryostat, detector, experimental setup, and x-ray source, along with the ion-implantation process performed at the RISIKO mass spectrometer at the Mainz University.

Chapter 6 then contains the results for this experiment. At first, the detector performance is characterised using noise and magnetisation measurements. The results for the heat capacity measurement are then analysed and discussed in comparison with the numerical results of chapter 4.

2. Direct determination of neutrino mass using ^{163}Ho

2.1 Massive neutrinos

The discovery of neutrino oscillations [Fuk98], a change of the neutrino flavour state between its creation and detection, showed that neutrinos must be massive particles whose flavour eigenstates are a superposition of mass eigenstates. This can be expressed by relating the 3 flavour eigenstates to 3 mass eigenstates via a unitary mixing matrix U:

$$\begin{pmatrix} \nu_e \\ \nu_\mu \\ \nu_\tau \end{pmatrix} = \begin{pmatrix} U_{11} & U_{12} & U_{13} \\ U_{21} & U_{22} & U_{23} \\ U_{13} & U_{32} & U_{33} \end{pmatrix} \cdot \begin{pmatrix} \nu_1 \\ \nu_2 \\ \nu_3 \end{pmatrix} \tag{2.1}$$

Experiments with solar neutrinos, reactor neutrinos, atmospheric neutrinos and accelerator neutrinos have precisely measured the mixing angles and the differences of the squared mass eigenvalues. However, neutrino oscillation experiments can be interpreted as interference experiments and as such can not give the absolute mass scale. To obtain the mass scale, three approaches are pursued, which measure different observables [Dre13].

Cosmology: Massive neutrinos had an impact on the structure formation from density fluctuations in the very early universe. Neutrinos with masses in the eV and sub-eV range are considered hot dark matter, which smears out density fluctuations at a scale that is dependent on the exact neutrino mass. Satellite base precision experiments on the cosmic microwave background (CMB), such as WMAP [Kom11] and Planck [Pla13] provide information on these density fluctuations in the early universe. By comparing these fluctuations to the current distribution of visible matter with large galaxy surveys like SDSS [Aih11], the influence of neutrinos on structure formation can be extracted. The observable for this method of measurement is given by the direct sum of the individual neutrino masses

$$m_\mathrm{C} := \sum_i m(\nu_i) \tag{2.2}$$

This method is, however, model- and analysis dependent, resulting in varying upper limits for m_C. Current upper limits are in the order of $m_\mathrm{C} < 0.5\,\mathrm{eV}$ [Dre13].

Neutrinoless double β-decay ($0\nu\beta\beta$): If neutrinos are their own anti-particles ("Majorana -neutrino" as opposed to the "Dirac-neutrino" of the standard model of particle

physics), the two neutrinos produced in a double β-decay could annihilate each other, resulting in an effectively neutrinoless double β-decay. The half life for such a decay follows from [Giu12] as

$$T_{1/2}^{0\nu\beta\beta} \propto |M^{0\nu\beta\beta}| m_{\mathrm{ee}}^2 \tag{2.3}$$

with the nuclear matrix element $M^{0\nu\beta\beta}$ and the effective Majorana neutrino mass given by

$$m_{\mathrm{ee}}^2 := \left| \sum_i U_{ei}^2 m(\nu_i) \right|^2 \tag{2.4}$$

where U_{ei} are elements of the neutrino mixing matrix and $m_(\nu_i)$ the neutrino mass eigenstates. Due to the coherent nature of the neutrino mass contribution to the half-life, the sum for m_{ee} carries the relative phases present in the mixing matrix. The search for the Majorana neutrino mass is pursued by measuring the $2e^-$ spectra of different isotopes, such as ^{76}Ge or ^{136}Xe, and precisely analysing the end point region, where a peak is expected at $E = Q_{\beta\beta}$, with $Q_{\beta\beta}$ the total decay energy, in case of neutrino-less events. A significant uncertainty in these measurements is caused by the nuclear matrix element relating the measured half life to the neutrino mass. One claim for evidence of a neutrino mass of $m_{\mathrm{ee}} \approx 0.3\,\mathrm{eV}$ with $T_{1/2}^{0\nu\beta\beta} \approx 1.2 \times 10^{25}\,\mathrm{yrs}$ for ^{76}Ge was made by the Heidelberg-Moscow collaboration [KK06]. This has been challenged by different experiments in the same range, e.g. the GERDA experiment with a limit of $T_{1/2}^{0\nu\beta\beta} > 2.1 \times 10^{25}\,\mathrm{yrs}$ at 90 % CL for ^{76}Ge [Ago13] and the EXO-200 experiment with a limit of $T_{1/2}^{0\nu\beta\beta} > 1.6 \times 10^{25}\,\mathrm{yrs}$ at 90 % CL for ^{136}Xe [Aug12]. The next generation of these experiments aims to reach a sensitivity for the effective Majorana mass of $m_{\mathrm{ee}} \approx 20\,\mathrm{meV}$ [Art14].

Direct neutrino mass determination:

In this approach, the neutrino mass is determined purely via kinematics. Two types of experiments fall into this category: Time-of-flight measurements and precision investigations of β- and electron capture decays. In the former, the difference in time-of-flight of massive neutrinos and massless photons is measured. As this difference is very small for the low neutrino mass, this method requires extremely long baselines and strong sources, both of which cannot be achieved on Earth and require cataclysmic events like a Type-II supernova. The current limit from this method is given by the supernova explosion SN1987a with 5.7 eV (95 % C.L.) [Lor01] or 5.8 eV (95 % C.L.) [Pag10], depending on the supernova model. While sub-eV sensitivities around 0.8 eV (95 % C.L.) are possible in ideal circumstances [Pag10], the still not sufficient knowledge of the star's behaviour during the supernova explosion is a significant disadvantage of this method.

The kinematic investigation of weak decays, specifically the end-point region of the β-decay or electron capture spectrum, can be carried out in laboratory based exper-

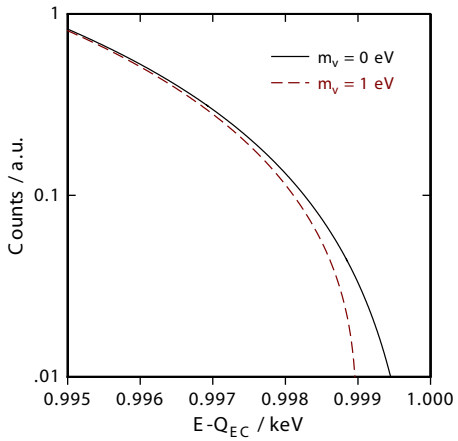

Figure 2.1: Difference between vanishing neutrino mass and an assumed neutrino mass ($m(\nu_\mathrm{e}) = 0\,\mathrm{eV}$) is shown for a general case of the endpoint region in a β- or electron capture decay. Q_EC is the energy available to the decay.

iments and does not make any further assumptions on the neutrino's nature. It is to date the most sensitive model-independent and direct method to determine the neutrino mass, with the limit of $m(\bar{\nu_e}) < 2.0\,\mathrm{eV}$ (95 % C.L.), given by the Mainz-Troitsk experiment [Ber12].

The neutrino mass influences the shape of the spectrum through the phase space term. The influence of the neutrino on the shape of the β- and electron capture decay spectra is dominant in the end-point region, as shown in figure 2.1, and given by the phase space term

$$\frac{dW}{dE} \propto (Q_\mathrm{EC} - E)^2 \sqrt{1 - \frac{m(\nu_\mathrm{e})^2}{(Q_\mathrm{EC} - E)^2}} \tag{2.5}$$

where Q_EC is the decay energy given by the mass difference between the parent nucleus and daughter nucleus of the decay. The observable neutrino mass in this case is given by the "average neutrino mass"

$$m(\nu_\mathrm{e})^2 := \sum_i \left|U_{ei}^2\right| m(\nu_i)^2 \tag{2.6}$$

where the mass eigenstates add incoherently in contrast to m_{ee} in $0\nu\beta\beta$-decay (see equation 2.4), which means that the phases in the mixing matrix U do not enter into the sum. From equation 2.5 follows, that the highest sensitivity for the neutrino mass is given in decays with low Q_EC. Using isotopes with a low Q_EC is therefore a central aspect for experiments using this method.

In a beta decay to the ground state, a neutron in the nucleus decays into a proton, emitting an electron and an electron anti-neutrino:

$${}^A_Z X \longrightarrow {}^A_{Z+1} X + e_- + \bar{\nu}_\mathrm{e} \tag{2.7}$$

Due to its large mass, the nucleus takes almost no energy from the decay and the energy is divided between electron and electron anti-neutrino. Experiments investigating β-decays are therefore sensitive to the mass of the electron anti-neutrino $\bar{\nu}_\mathrm{e}$ by measuring the energy of the emitted electron. The most commonly used source is the heavy hydrogen isotope tritium ^{3}H, with $Q_\mathrm{EC} = 18.6\,\mathrm{keV}$. It was used in the previously mentioned Mainz-Troitsk experiment and will be employed in its successor experiment KATRIN[1] [Ang05], which is intended to start taking data in 2016 and reach a sensitivity of $m(\bar{\nu}_\mathrm{e}) \approx 0.2\,\mathrm{eV}$.

In an electron capture decay, a proton in the nucleus captures an electron, a neutron is formed and an electron neutrino ν_e is emitted. The daughter atom is left in an excited state, due to the hole in the electronic orbital from which the electron was captured and an additional electron in the external shell. The de-excitation then follows by the emission of x-rays, Auger electrons and Coster-Kronig transitions, which can be detected. The process can be written in the following two steps

$$\begin{aligned} {}^{A}_{Z}X &\longrightarrow {}^{A}_{Z-1}X^{*} + \nu_e \\ &\hookrightarrow {}^{A}_{Z-1}X + Q_\mathrm{EC} \ , \end{aligned} \tag{2.8}$$

describing the decay to the nuclear ground state.

In contrast to the β-decay, where an electron anti-neutrino $\bar{\nu}_e$ is emitted, the experiments on electron capture decays are sensitive to the mass of the electron neutrino ν_e. Due to the uncertainty in branching ratios and complicated de-excitation schemes, measuring single electrons or x-rays is not sufficient for a high sensitivity neutrino mass measurement. The optimal solution is that the whole decay energy, except that of the neutrino, is measured. This can be achieved by embedding the source directly into a detector with high energy resolution and a high quantum efficiency for the emitted radiation. Such a detector can be a calorimeter, where the particles emitted in the decay deposit their energy in an absorber, causing a temperature increase based on the first law of thermodynamics

$$\Delta T = \frac{E}{C_\mathrm{tot}} \tag{2.9}$$

where C_tot is the heat capacity of the calorimeter and E the total energy of the decay emitted via electrons and x-rays.

The main isotope of interest for neutrino mass experiments on electron capture is ^{163}Ho in the ECHo[2] [Gas14], HOLMES[3] [Alp15] and NUMECS[4] [Kun14] experiments.

[1] Karlsruhe Tritium Neutrino experiment

[2] Electron Capture in ^{163}Ho Experiment

[3] The Electron Capture Decay of ^{163}Ho to Measure the Electron Neutrino Mass with sub-eV sensitivity

[4] Neutrino Mass via Electron Capture Spectroscopy

2.2 Electron Capture in ^{163}Ho experiment

The Electron Capture in ^{163}Ho Experiment, ECHo, is a direct neutrino mass experiment investigating the weak decay of the Holmium isotope ^{163}Ho. A sensitivity to the electron neutrino mass below 1 eV can be reached through a high precision and high statistics calorimetric measurement of the electron capture spectrum. ^{163}Ho decays to ^{163}Dy expressed as

$$\begin{aligned} {}^{163}_{67}Ho &\longrightarrow {}^{163}_{66}Dy^{*} + \nu_e \\ &\hookrightarrow {}^{163}_{66}Dy + Q_{\mathrm{EC}} \ , \end{aligned} \tag{2.10}$$

with a half-life of $\tau_{1/2} = 4570\,\mathrm{y}$, corresponding to $\sim 2 \times 10^{11}$ atoms/Bq. The recommended value for the energy available to the decay is $Q_{\mathrm{EC}} = (2.555 \pm 0.016)\,\mathrm{keV}$ [Wan12], however, the measured value varies significantly between individual measurements, ranging between $Q_{\mathrm{EC}} \approx 2.3\,\mathrm{keV}$ [And82] and $Q_{\mathrm{EC}} \approx 2.8\,\mathrm{keV}$ [Gat97][Ran14]. An independent measurement of Q_{EC} by means of Penning trap mass spectrometry is planned by measuring the ^{163}Ho and ^{163}Dy mass at the newly developed PENTATRAP at the MPIK[5] [Rep12][Rou12]. It will be possible to determine Q_{EC} with 1 eV precision.

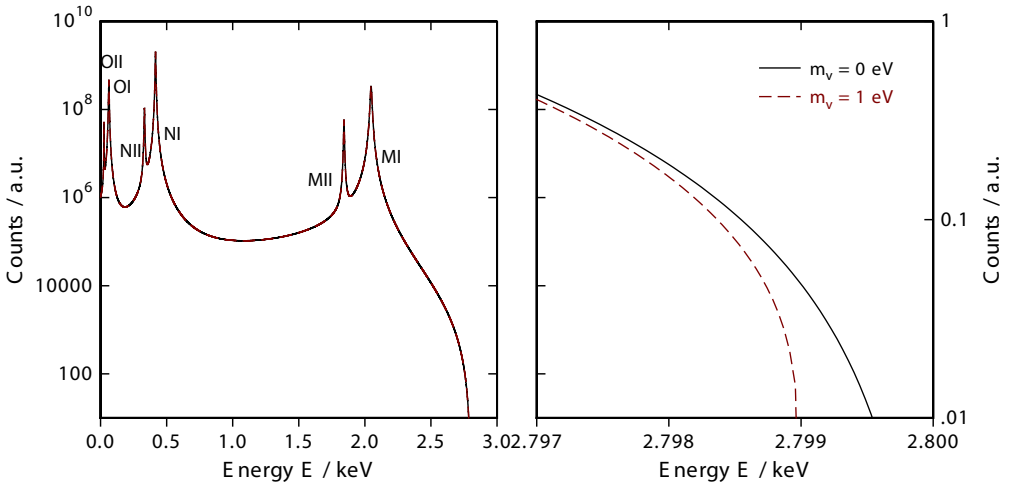

Figure 2.2: Theoretical spectrum of the electron capture decay in ^{163}Ho including only first-order excitations (left) and zoom on the end-point region for $m(\nu_{\mathrm{e}}) = 0\,\mathrm{eV}$ and $m(\nu_{\mathrm{e}}) = 1\,\mathrm{eV}$

For first order excitations, where only the one hole left by the captured electron is

[5]Max-Planck Institut für Kernphysik - Max-Planck Institute for Nuclear physics in Heidelberg, Germany

considered, the spectrum is shown in figure 2.2 and is given in [De 82] as

$$\frac{dW}{dE} = A(Q_{\mathrm{EC}} - E)^2 \sqrt{1 - \frac{m(\nu_{\mathrm{e}})^2}{(Q_{\mathrm{EC}} - E)^2}} \sum_H B_H \phi_H^2(0) \frac{\frac{\Gamma_{\mathrm{H}}}{2\pi}}{(E_{\mathrm{C}} - E_H)^2 + \frac{\Gamma_H^2}{4}}, \qquad (2.11)$$

where the phase space term (equation 2.5) is multiplied by a constant A including the nuclear matrix element, and a sum of Breit-Wiegner resonances, one for each electronic state where a hole is created in the decay. The latter is characterized by relative amplitudes of the transitions, given in first approximation by the electron's wave function at the origin $\phi_{\mathrm{H}}^2(0)$, the exchange and overlap corrections B_{H}, and their Lorentzian function, described by the line's central energy position E_{H} and its width Γ_{H}.

A more precise description of the spectral shape can be found in [Fae14, Fae15a, Fae15b], where a complete relativistic approach has been used to calculate the amplitude of the lines, as well as the effects on the spectral shape due to excitations of higher order, including two holes and three holes in the Dy-atom after electron capture. The effects due to 2-holes excitations can give contributions below the 1 % level while the 3-holes excitations contribution is much lower.

To reach a sub-eV sensitivity on the ν_e mass it is important to measure the ^{163}Ho spectrum with high precision. The best choice for this measurement are low temperature micro-calorimeters, which can reach energy resolutions below $\Delta E_{\mathrm{FWHM}} = 2\,\mathrm{eV}$ and a quantum efficiency of 100 % below 3 keV [Fle05]. In a micro-calorimeter, the calorimetric principle is used (see equation 2.9) to measure energy through the associated temperature change ΔT. To achieve a significant ΔT for energies $E < 3\,\mathrm{keV}$ very small heat capacities are required. To this end, very small detectors in the $\mu\mathrm{m}^3$-range are used at cryogenic temperatures of $T < 100\,\mathrm{mK}$, utilizing the heat capacity's temperature dependence

$$C \propto T^3 \qquad (2.12)$$

given by Debye's law.

In the ECHo experiment metallic magnetic calorimeters (MMC), which are described in detail in chapter 3, will be used, where ^{163}Ho is embedded in the detector absorbers, achieving a quantum efficiency > 99 %. Using a first prototype of an MMC with embedded ^{163}Ho , the ECHo collaboration has already shown that MMCs are suitable for the high resolution measurement of the ^{163}Ho spectrum [Ran14] (see chapter 3.5).

2.2.1 Sensitivity

According to equation 2.11, the interesting events for neutrino mass determination are located in the end-point region of the spectrum. To reach sub-eV sensitivity for

the neutrino mass, it is important to:

- have detectors with an energy resolution of $\Delta E_{\mathrm{FWHM}} < 2\,\mathrm{eV}$.
- reduce background events below the statistical uncertainty of the ^{163}Ho counts.
- have a suitable expected number of counts.

The required energy resolution can be achieved with metallic magnetic calorimeters, which will be discussed in chapter 3.

The background in the experiment is due to muons, natural radioactivity, radioactive contaminations of the source and the intrinsic background caused by unresolved pile-up events. Muons and natural radioactivity can be suppressed with muon vetos and material screening, and by moving the experiment to an underground facility. Source contaminations can be removed using chemical separation processes [Due15]. The aim of the ECHo experiment is to reduce the external background to a level that is smaller than an unresolved pile-up fraction of $f_{\mathrm{pu}} \approx 10^{-6}$. Unresolved pile-up events

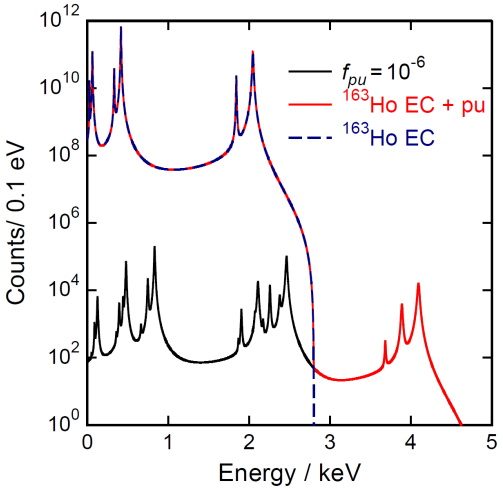

Figure 2.3: Theoretical spectrum of the electron capture decay in ^{163}Ho with (red) and without (blue) unresolved pile-up events with the unresolved pile-up fraction (black) $f_{\mathrm{pu}} = 10^{-6}$.

occur, when two or more events occur in the detector within a time interval smaller than the detector rise-time τ. The unresolved pile-up fraction with respect to the total number of counts can be calculated as

$$f_{pu} = A \cdot \tau \tag{2.13}$$

where A is the activity of ^{163}Ho in a detector. Since pile-up events distort the theoretical spectrum predominantly in the end-point region (see figure 2.3), the fraction of these events need to be kept as small as possible.

In the case of $Q_{\mathrm{EC}} = 2.8\,\mathrm{keV}$, the fraction of events in the last eV below Q_{EC} is about 6×10^{-13}. To investigate the ν_e-mass in the sub-eV range, more than 10^{14} events

in the full spectrum need to be considered. To measure this number of events in a reasonable time of $T = 1\,\mathrm{y}$, would require a total activity of a few MBq. By using multiple detectors, the total number of events can be expressed as

$$N_{tot} = A \cdot n \cdot t \tag{2.14}$$

with A the activity per detector, n the number of detectors and t the measuring time. The activity per pixel is heavily limited by two factors: unresolved pile-up events leading to an intrinsic background in the spectrum as discussed previously, and the contribution of holmium ions to the detector's heat capacity, which reduces the signal size associated with an event.

As the ECHo experiment aims for an unresolved pile-up fraction of $f_{pu} < 10^{-5}$, taking a rise-time of $\tau \approx 100\,\mathrm{ns}$ and equation 2.13 results in an upper limit for the ^{163}Ho activity per pixel of $A \approx 10\,\mathrm{Bq}$. This means, that 10^5 detectors need to be read out in parallel to measure a total activity of $A_{tot} \approx 1\,\mathrm{MBq}$, leading to the ongoing development of multiplexed SQUID-readout for cryogenic micro calorimeters [Weg13][Kem14].

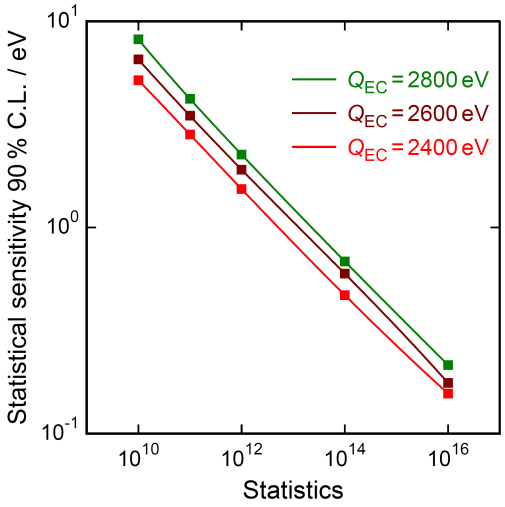

Figure 2.4: Sensitivity of neutrino mass determination as function of the total decay count, given for three possible values of Q_{EC}

Holmium ions carry a magnetic dipole moment of $\mu = 10.6\mu_{\mathrm{B}}$, which is the largest of any rare-earth element. Embedding these large dipole moments into the gold absorber introduces an additional heat capacity C_{Ho} into the thermodynamic system. Equation 2.9 then follows as

$$\Delta T = \frac{E}{C_{\mathrm{tot}}} = \frac{E}{C_{\mathrm{det}} + C_{\mathrm{Ho}}} \tag{2.15}$$

where C_{det} is the heat capacity of the detector without considering the presence of Ho-ions, and C_{Ho} is the heat capacity related to the Ho-ion in the absorber material. It can be calculated by defining a specific heat per Ho-ion. Increasing the ^{163}Ho

activity per detector, and therefore the number of ions, introduces a higher heat capacity into the system. This decreases the temperature change due to an event and consequently the signal-to-noise ratio. This leads to a decreased energy resolution of the detector, which sets a separate upper limit on the possible ^{163}Ho activity per pixel, independent from the limit set by the unresolved pile-up fraction.

The aim of this thesis is to develop a method to define the optimal activity per pixel by compromising between a low unresolved pile-up fraction and the maximal activity for which the heat capacity of the Ho-ions C_{Ho} is smaller than C_{det}.

3. Principles of metallic magnetic calorimeters

3.1 Detection principle

Metallic magnetic calorimeters (MMC) are energy dispersive, cryogenic particle and x-ray detectors based on the calorimetric principle introduced in section 2.1. In figure 3.1 the essential parts of such a metallic magnetic calorimeter are shown.

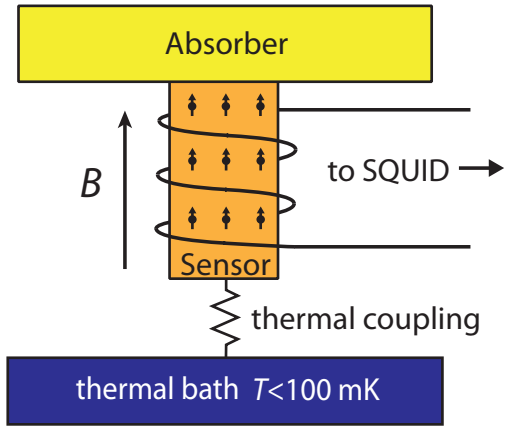

Figure 3.1: Schematic of a metallic magnetic calorimeter. It shows the absorber coupled to the paramagnetic sensor, which is in turn weakly coupled to the thermal bath. A magnetic field B is applied to the sensor, and a superconducting coil surrounding the sensor is connected to the read-out SQUID.

Particles hitting the detector are stopped in a suitable absorber where they deposit their energy. The absorber is connected via a strong thermal link to a paramagnet sitting in a weak magnetic field, which serves as a temperature sensor and is in turn weakly coupled to a thermal bath. The applied magnetic field causes a temperature dependent magnetisation in the paramagnet, which is detected by superconducting pick-up coil coupled to the paramagnet. A SQUID-magnetometer inductively coupled to the pick-up coil then amplified the change in magnetic flux and translates it into a voltage signal.

The deposited energy E causes an initial temperature rise in the absorber and the paramagnetic sensor given by equation 2.9 (see section 2.1). Due to weak coupling with the thermal bath, the system then relaxes back to its initial state with the relaxation time τ_1 defined by the thermal link G:

$$\tau_1 \approx \frac{C_{\mathrm{tot}}}{G} \tag{3.1}$$

Any temperature change causes a magnetisation change in the temperature sensor, leading to a change in magnetic flux

$$\delta\Phi \propto \frac{\partial M}{\partial T}\delta T = \frac{\partial M}{\partial T}\frac{E}{C_{\mathrm{tot}}} \tag{3.2}$$

through the superconducting pick-up coil. Since the flux through a closed superconducting loop is a conserved quantity, a current

$$\delta I \propto \delta\Phi \propto E \tag{3.3}$$

is induced in the pick-up coil which creates a magnetic field of equal magnitude but opposite to the field change caused by the paramagnet. This screening current is detected by using a SQUID-magnetometer (see section 3.4) and serves as a measurable variable proportional to the absorbed event energy.

3.2 Signal size

The signal size of an MMC is given by the flux change in the SQUID-magnetometer and can written as

$$\Delta\Phi_{\mathrm{S}} = k_{\Phi}\frac{\partial M}{\partial T}\frac{E}{C_{\mathrm{tot}}} \tag{3.4}$$

where k_{Φ} is the flux coupling between pick-up coil and SQUID-magnetometer. The signal size is dependent on the total heat capacity of the detector, which can be written as

$$C_{\mathrm{det}} = C_{\mathrm{e}} + C_{\mathrm{ph}} + C_{\mathrm{z}} \tag{3.5}$$

where C_{e} is the electronic and C_{ph} the phononic heat capacity of the gold in absorber and sensor. C_{z} is the heat capacity of the spin-system of the paramagnetic Er-ions in the Au:Er -sensor, which is also called Zeeman-system. For temperatures lower than the Debye temperature $T << \Theta_{\mathrm{D}}$ ($\Theta_{\mathrm{D}} = 164\,\mathrm{K}$ for gold), the electronic and phononic heat capacities behave as

$$C_{\mathrm{e}} = \frac{V}{V_{\mathrm{vol}}}\gamma T \tag{3.6}$$

$$C_{\mathrm{ph}} = \frac{V}{V_{\mathrm{vol}}}\frac{12\pi^4}{5}R\left(\frac{T}{\Theta_{\mathrm{D}}}\right)^3 \tag{3.7}$$

with the Sommerfeld coefficient γ ($\gamma = 0.729\,\mathrm{mJ/mol\,K^2}$ for bulk gold),the ideal gas constant $R \approx 8.31\,\mathrm{J/mol\,K}$, V_{mol} is the molar volume ($V_{\mathrm{mol,Au}} = 1.2 \times 10^{-5}\,\mathrm{mol/m^3}$) and V the combined volume of absorber and sensor. At temperatures $T < 100\,\mathrm{mK}$, the phononic heat capacity C_{ph} is about three orders of magnitude smaller than the electronic heat capacity C_{e} and therefore negligible.

The heat capacity of the sensor's Zeeman-system C_{z} is dependent on the temperature, applied magnetic field and the Er-ion concentration and is calculated numerically. A numerical description for interacting Er-ions was shown to allow calculations of C_{z} at a high degree of accuracy (see figure 3.2). A detailed description of the properties of Au:Er has been compiled by graduate students of our group and can be found in appendix A.

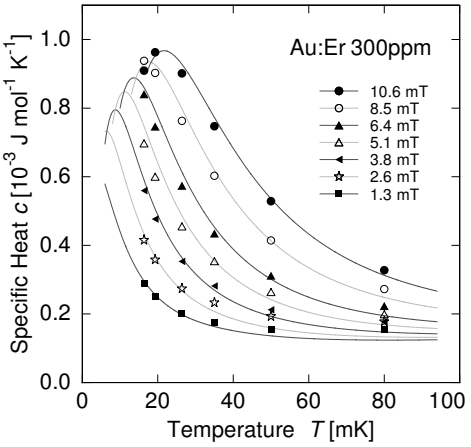

Figure 3.2: Specific heat capacity of Au:Er with 300 ppm enriched ^{166}Er as a function of temperature at different applied fields. The solid lines are calculated numerically [Ens05].

3.2.1 Signal shape

The description of the signal size in the previous section does not include the time dependent thermalisation of the detector. To describe the time dependent behaviour of the signal size, a metallic magnetic calorimeter can be characterized as a canonical ensemble, shown in figure 3.3. The thermodynamic system of a metallic magnetic calorimeter can be described as a canonical ensemble with two sub-systems, as shown in figure 3.3. The sub-systems are given by the Zeeman system of the magnetic moments and the electrons of the conduction band, with heat capacities C_z and C_e as discussed in the previous section. The two systems are thermally coupled by a coupling G_ez, with an additional thermal coupling G_eb between the system of the conduction electrons and the thermal bath. Two noise sources $P_\mathrm{ez}(t)$ and $P_\mathrm{eb}(t)$ are shown in parallel to the thermal links and are used to describe the random energy fluctuations between the systems in thermal equilibrium [Pie12a].

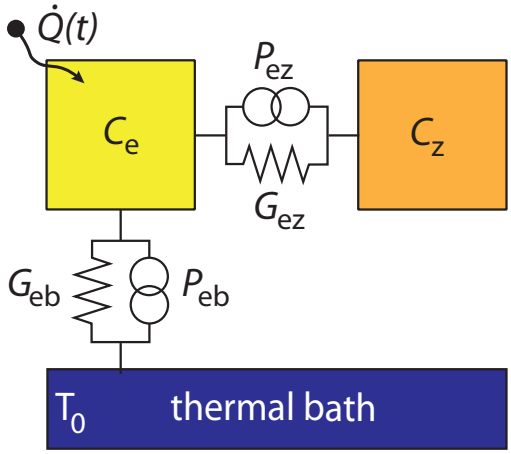

Figure 3.3: Schematic of a double meander pick-up coil. The direction of the magnetic field is indicated with symbols.

The time dependence of the temperatures T_e and T_z of the two sub-system can now

be described with two coupled differential equations [Pie12a]

$$C_z\dot{T}_z = \quad (T_e - T_z)G_{ez} + P_{ez} \tag{3.8}$$

$$C_e\dot{T}_e = -(T_e - T_z)G_{ez} - P_{ez} - (T_e - T_b)G_{eb} - P_{eb} + \dot{Q}(t) \tag{3.9}$$

where equations 3.8 and 3.9 describe the heat flow to the Zeeman system and the electronic system respectively. External sources of thermal energy are included with the term $\dot{Q}(t)$. By using the Dirac delta function to describe the absorption of a particle with energy E

$$\dot{Q}(t) = E\delta(t) \tag{3.10}$$

and neglecting the noise sources P_{ez} and P_{eb}, a solution for the energy $E_z(t)$ contained in the Zeeman system can be found from the differential equations as a function of time,

$$E_z(t) = E_z T_z(t) = E\beta(e^{-t/\tau_1} - e^{-t/\tau_0}). \tag{3.11}$$

with $\beta = C_z/(C_z + C_e)$. The time constants τ_0 and τ_1 describe the thermal relaxation between the sub-systems and are dependent on the thermal couplings G_z and G_e, as well as the heat capacities of the systems. The rise time of the signal is given by the Korringa relation [Whi02]

$$\tau_0 = (1 - \beta)\frac{\kappa}{T_e} \tag{3.12}$$

where $\kappa = 7 \times 10^{-9}\,\mathrm{Ks}$ for Au:Er [Sjø75]. For $\beta \approx 0.5$ and $T = 50\,\mathrm{mK}$ a rise time of $\tau_0 \approx 100\,\mathrm{ns}$ can be found.

The possibility to predict the signal size in MMC with high confidence opens the way to design detectors with optimized geometries for well defined applications. In this thesis, the reliable understanding of the signal size of metallic magnetic calorimeters is used to detect deviations from the expected behaviour, due to the presence of Ho-ions in the absorber.

3.3 Read-out geometry

Well established MMC geometries are based on planar Au:Er temperature sensors, which are compatible with micro-fabrication processes for complete detectors. The pick-up coil in an MMC serves two purposes: Detect magnetisation changes in the paramagnetic sensor and create the magnetic field which polarizes the sensor spins. Presently two geometries are commonly used in the fabrication of MMC: The double-meander geometry and the sandwich geometry [Heu11]. In this work, MMC with meander geometry have been used.

The double-meander configuration is shown in figure 3.4. The coils are generally made of niobium, which is superconducting below the critical temperature of $T_c \approx$

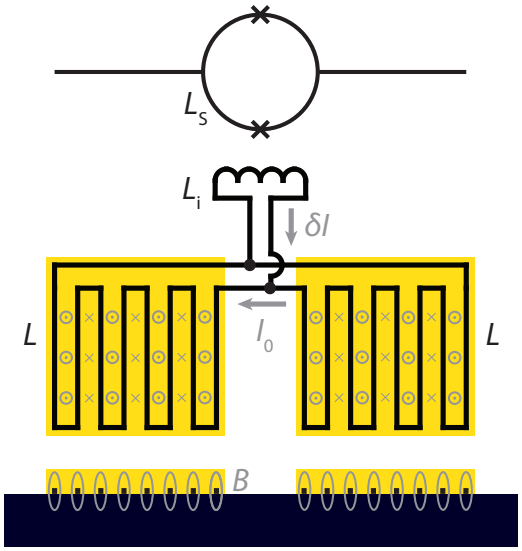

Figure 3.4: Schematic of a double meander pick-up coil. The direction of the magnetic field is indicated with symbols.

9.25 K. Two pick-up coils with inductance L are connected in parallel to the input coil of the SQUID with inductance L_i, which is inductively coupled to the SQUID-magnetometer. Since the pick-up coils have opposite winding, they form a first-order gradiometer which is insensitive to external magnetic field fluctuations. Au:Er is deposited on top of the meander, with a height h of about 1/3 of the meanders pitch p (see 3.5).

The magnetic field generated by the current in the meander is highly inhomogeneous and decays exponentially in the z-direction. This optimizes the magnetic coupling between coil and sensor [Fle09], while significantly reducing the magnetic field strength in the absorber. The low magnetic field strength of $B < 0.1\,\mathrm{mT}$ makes it possible to neglect the effect of the magnetic field on the thermodynamic properties of the Ho-ions embedded in the absorber, which are discussed in chapter 4.

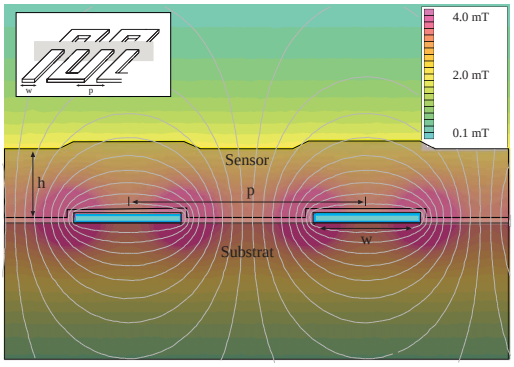

Figure 3.5: Cross section through a magnetic calorimeter with substrate, meander shaped pick-up coil, sensor and absorber. The magnetic field lines are illustrated by grey lines, the magnitude of the magnetic field is given by different shades of colours [Seg09].

When Au:Er covers both pick-up coils, the configuration is insensitive to the absolute temperature of the chip, as magnetisation changes occurring in both sensors cancel each other out. This allows for a more stable operation of the detector, and the two sensors can be equipped with absorbers, doubling the detection area of the detector.

However, this slightly increases the noise, as the thermodynamic noise from both detectors couple incoherently as flux noise in the SQUID.

When only one pick-up coil is covered with Au:Er, the detector becomes sensitive to the temperature change of the substrate and therefore it is possible to measure the magnetisation M as function of temperature of the single sensor.

The current I_0 generating the magnetic field of in the paramagnetic sensor is a persistent current stored in the superconducting loop consisting of the two meanders. This current is injected using a heat switch, which is fabricated on the detector chip.

3.4 dc-SQUID magnetometer

For this thesis, dc-SQUID[1] magnetometers were used for the read-out of the detector signal. A brief introduction of the relevant principles of a SQUID is given in this chapter, while a detailed description of SQUIDs can be found in [Cla04].

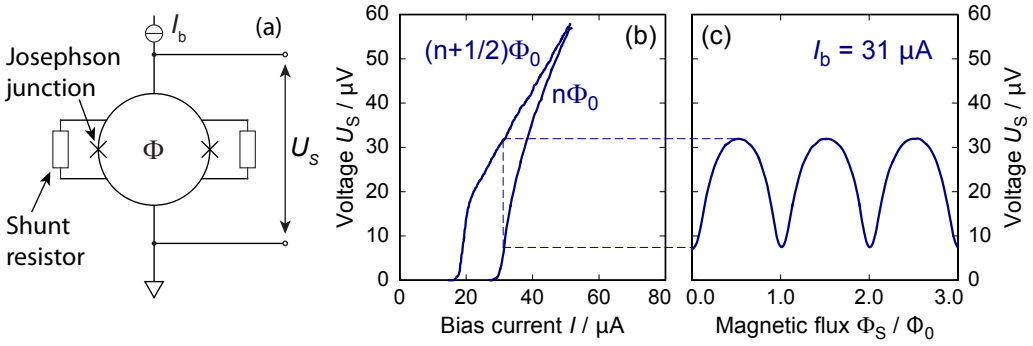

Figure 3.6: **a)** Schematic representation of a dc-SQUID magnetometer. **b)** Current-voltage characteristic for $\Phi = n\Phi_0$ and $\Phi = (n + 1/2)\Phi_0$. **c)** Voltage drop in the SQUID for constant current as a function of magnetic flux.

As figure 3.6a) shows, a dc-SQUID consists of a superconducting loop, which is interrupted by two Josephson junctions consisting of thin, normal conducting layers. The macroscopic wave functions of the Cooper-pairs in the two halves of the loop are lightly coupled through the thin layers, which allows coherent tunneling of Cooper-pairs through the barrier. Two shunt resistances are connected in parallel to the Josephson contacts, to avoid hysteretic behaviour of the voltage-current characteristic [McC68].

A bias current I_b is injected into the SQUID. For I_b smaller than twice the critical current I_c of a Josephson junction, lossless tunneling (no voltage drop) of Cooper-pairs through the junctions is possible [Jos62]. For $I_\mathrm{b} \leq 2I_\mathrm{c}$ the SQUID shows ohmic

[1] **Su**perconducting **Qu**antum **I**nterference **D**evice

behaviour. The resulting current-voltage characteristic is shown in figure 3.6b) and can be described by

$$U_\mathrm{S} = \frac{R}{2}\sqrt{I_\mathrm{b}^2 - \left[2I_\mathrm{c}\cos\left(\frac{\Phi}{\pi\Phi_0}\right)\right]} \tag{3.13}$$

with the magnetic flux through the SQUID Φ_S, the magnetic flux quantum $\Phi_0 = 2.07 \times 10^{-15}\,\mathrm{Vs}$ and the resistance of the two shunt resistances R. For a given bias current $I_\mathrm{b} \leq 2I_\mathrm{c}$, the voltage drop over the Josephson junctions is dependent on the magnetic flux through the SQUID, with maxima at $\Phi = (n + 1/2)\Phi_0$ and minima at $\Phi = n\Phi_0$, $n \in \mathbb{N}$. The resulting flux-voltage characteristic is shown in figure 3.6b). The slope $V_\Phi = \delta U/\delta\Phi$ at the point of inflection is a measure for the sensitivity of the SQUID in regard to flux changes.

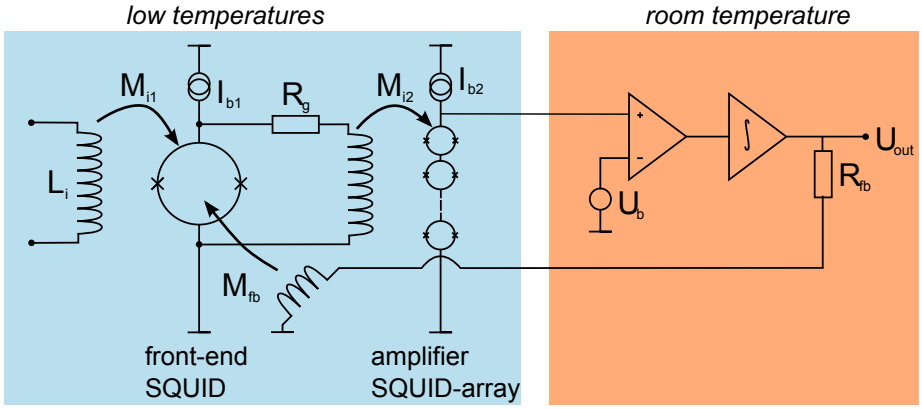

Figure 3.7: Schematic representation of a two stage SQUID setup including the flux-locked-loop circuit at room temperature.

Due to the periodic characteristic, unique mapping between flux and voltage values is impossible for flux changes $\Delta\Phi > \Phi_0/2$. To avoid this issue, a feedback circuit is used, where the voltage signal is amplified, integrated and inverted at room temperature. This signal is subsequently fed back to the SQUID through an inductively coupled feedback coil. This stabilizes the magnetic flux in the SQUID at a working point positioned at a point of inflection in the flux-voltage characteristic.

This so-called flux-locked-loop (FLL) circuit is shown in figure 3.7. A two-stage SQUID setup is shown, where the first stage consists of the so-called front-end SQUID, which is connected to the MMC. The second stage consists of 16 SQUIDs connected in series and serves as a low-T amplifier, which has the advantage of a low-noise signal amplification [Kra13]. The voltage U across the feedback resistor R_fb is used as the output signal of the circuit and is given by

$$U = \frac{R_\mathrm{fb}}{M_\mathrm{fb}}\Delta\Phi_\mathrm{S} \tag{3.14}$$

with the mutual inductance M_{fb} between feedback coil and front-end SQUID and the flux change $\Delta\Phi_{\mathrm{S}}$ in the front-end SQUID.

3.5 First prototype metallic magnetic calorimeters with implanted ^{163}Ho

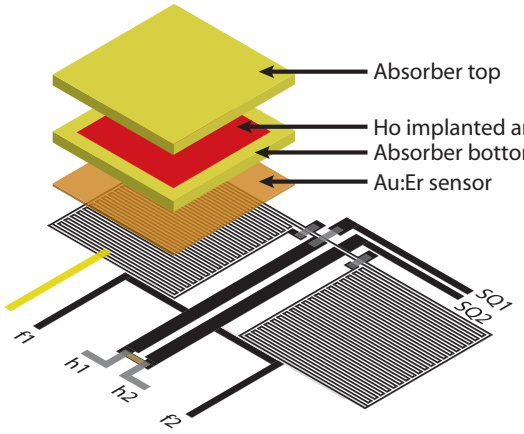

Figure 3.8: Schematic of one detector on the prototype chip.

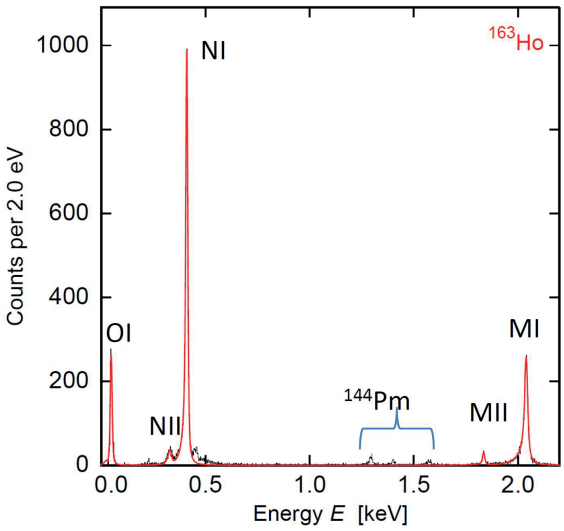

Figure 3.9: Measured spectrum of ^{163}Ho electron capture with theoretical fit in red. Peaks are labelled according to the corresponding electronic transitions.

A prototype MMC detector with embedded ^{163}Ho was micro-fabricated in the cleanroom of the Kirchhoff-Institute for Physics [Gas13]. Each micro-fabricated chip consists of four detectors, with the schematic of a single MMC detector shown in figure 3.8. The MMC consists of two meander shaped coils in a gradiometric setup, with electrical connections for the input coil of the SQUID, marked $SQ1$ and $SQ2$, and the heat switch with connections for heater current and field current marked $h1$,$h2$ and $f1$,$f2$ respectively. A Au:Er sensor of $190 \times 190 \times 1.3\,\mu\mathrm{m}^3$ is sputtered on one of the meanders, with a layer of gold sputtered on top of it, serving as absorber with a height of $5\,\mu\mathrm{m}$ and an area of $185 \times 185\,\mu\mathrm{m}^2$.

The radioactive ^{163}Ho is implanted at the ISOLDE[2] facility at CERN[3] [Kug00]. The ions are implanted directly into the gold absorber of each detector in an area of

[2]Isotope Seperator On-Line Device

[3]Conseil Européen pour la Recherche Nucléaire - European Organization for Nuclear Research in Geneva, Switzerland

$160 \times 160\,\mu\text{m}^2$ per absorber, which is defined by a photoresist layer covering the whole chip. After the implantation process, the photoresist layer is removed and a second gold layer of $185 \times 185 \times 5\,\mu\text{m}^3$ is deposited on top of the absorbers, completely encasing the holmium. This ensures a quantum efficiency of $> 99\,\%$.

The first prototype chip was produced in 2009 and implanted with a ^{163}Ho activity of only 0.01 Bq. Several measurements were carried out over the course of 4 years, showing no degradation over time. The resulting spectrum is shown in figure (3.9) with an energy resolution of $\Delta E_{\text{FWHM}} = 7.6\,\text{eV}$ and a signal rise time of $\tau \approx 100\,\text{ns}$. Radioactive source contaminations like the ^{144}Pm, which can be seen in the spectrum, can be removed by the chemical separation mentioned in chapter 2.2.1. While improvements on the performance of the detector are still necessary to reach the performance of $\Delta E_{\text{FWHM}} < 2\,\text{eV}$ and $\tau < 100\,\text{ns}$ needed for the sub-eV neutrino mass measurement (see chapter 2.2.1), this shows that MMCs are viable detectors for this kind of experiment.

4. Thermodynamic properties of holmium in gold

In the previous sections, it was shown that the implantation of ^{163}Ho is a promising way to embed the source in the absorber of an MMC, so that the quantum efficiency of 100 % is achieved. However, the thermodynamic properties of holmium in gold are not well known. In particular, the heat capacity C_{Ho} due to the presence of holmium in gold needs to be determined, because of its effect on the energy resolution of the MMC. Specifically the impact on the energy resolution due to the additional heat capacity C_{Ho} needs to be determined. In the following, a statistical approach is used to describe the thermodynamic propertuies of holmium ions in a gold matrix in the limit of very dilute alloys.

4.1 General properties of Ho^{3+}-ions

When holmium is implanted into gold, it occupies the place of a gold ion in the fcc crystal lattice (lattice constant $a_0 = 4.08\,\text{Å}$), as shown in figure 4.1 and loses three electrons to the de-localised electron system of the surrounding gold lattice. The resulting Ho^{3+}-ion has an electron configuration of $[\mathrm{Kr}]\,4d^{10}4f^{10}5s^25p^6$, which have a spatial extent of $R \approx 1\,\text{Å}$.

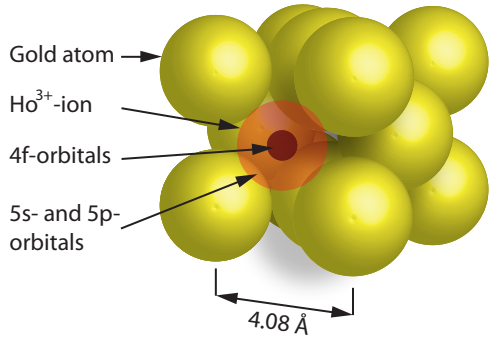

Figure 4.1: Schematic view of a crystal lattice section for Au:Ho. The Ho^{3+}-ion takes the regular place of a Au-atom in the Au-matrix. The $4f$-shell is located deep within the ion.

The electrons of the unfilled $4f$-shell carry a permanent magnetic moment, which causes the paramagnetic behaviour of holmium. This shell lies deep within the Ho-ion with a radius of $R \approx 0.3$ reducing the effect of the crystal field on the $4f$ electronic orbitals. This allows the use of Hund's rules to determine the spin-orbit coupling of the Ho^{3+}-ion and determine the angular momenta $\boldsymbol{L}$, $\boldsymbol{S}$ and $\boldsymbol{J}$. The magnetic moment $\boldsymbol{\mu}_{\mathrm{J}}$ then follows with the Landé factor

$$g_J = 1 + \frac{J(J+1) + S(S+1) - L(L+1)}{2J(J+1)} \tag{4.1}$$

and the relation

$$\boldsymbol{\mu}_\mathrm{J} = g_\mathrm{J}\mu_\mathrm{B}\boldsymbol{J} \tag{4.2}$$

where $\mu_\mathrm{B} = 9.274 \times 10^{-24}\,\mathrm{J/T}$ is the Bohr magneton. For Ho^{3+},$J = 8, L = 6, S = 2, g_\mathrm{J} = 4/3$, resulting in a magnetic moment of $\mu_\mathrm{J} = 10.6\mu_B$.

For the undisturbed magnetic moment, the energetic ground state would be 17-fold degenerated, due to the possible values of the magnetic quantum number

$$m_\mathrm{J} = -8, -7, \ldots, 0, \ldots, 7, 8 \tag{4.3}$$

ranging from $-J$ to $+J$. The excited states of the magnetic moment are given by the spin-orbit coupling on an energy scale of several thousand Kelvin. At temperatures below room temperature, the Ho^{3+}-ion therefore has a negligible probability to occupy an excited electronic state [Sch00], reducing it to a single-level system. A single-level system could not show thermodynamic properties like magnetisation and heat capacity, as these require multiple available energy states.

However, the degeneration of the ground state is generally broken by the influence of external fields, including a possible external magnetic field, the crystal field and the hyperfine interaction with the holmium nucleus. The effect of these are small compared to the given energy splitting and can be treated as perturbations on the ground state.

4.2 Zeeman effect

The simplest approach to break the degeneracy of the ground state levels is to consider an external magnetic field $\boldsymbol{B}$. This field breaks the spatial symmetry of the previously undisturbed Ho-ion. The 17-fold degeneracy of the ground state is therefore broken, with an energy splitting that can be described with the Zeeman effect, where the Hamiltonian is given by

$$H_\mathrm{Z} = g_\mathrm{J}\mu_\mathrm{B}\boldsymbol{B}\cdot\boldsymbol{J} \tag{4.4}$$

with energy eigenvalues of

$$E_\mathrm{Z} = g_\mathrm{J}\mu_\mathrm{B}|\boldsymbol{B}|m_\mathrm{J} \tag{4.5}$$

where $\boldsymbol{B} \parallel J_\mathrm{z}$ is used. The presence of these energy levels leads to a finite heat capacity and magnetisation. In the standard design of a metallic magnetic calorimeter, the magnitude of the magnetic field, generated by the persistent current flowing in the meander-shaped pick-up coil, is negligibly small in the absorber volume (see section 3.3) and has therefore no significant impact on the thermodynamic properties of Ho^{3+}-ions. The energy splitting due to earth's magnetic field is about $50\,\mu$K at $60\,\mu$T and therefore negligible.

4.3 Crystal field

4.3.1 Crystal field Hamiltonian

The crystal field effect on the Ho^{3+}-ion is caused by the electrostatic field of the surrounding Au-ions. In section 4.1 it was discussed that the influence of this crystal field does not break spin-orbit coupling, as the electronic orbitals of the $4f$-shell are deep inside the holmium atoms. While this is correct, the crystal field effect breaks the degeneration of the ground state on a non-negligible energy scale of about 10 K to 100 K and needs to be included in the calculation.

To describe the crystal field, the electric fields of the single ions are combined in one electrostatic potential having the symmetry of the crystal lattice. For the cubic symmetry of the gold fcc-lattice, the crystal field acting on the $4f$ shell can be described with a potential containing crystal field functions of fourth and sixth order.

The effect of this potential on the energy levels of the holmium ion can be calculated by transforming the crystal field functions in the potential to quantum mechanical operators of equivalent symmetry [Ste51]. The resulting Hamiltonian is then given by [Lea62] as

$$H_{\mathrm{CF}} = W\left[x\frac{\hat{O}_4^0 + 5\cdot\hat{O}_4^4}{F(4)} + (1-|x|)\frac{\hat{O}_6^0 - 21\cdot\hat{O}_6^4}{F(6)}\right] \tag{4.6}$$

where the crystal field operators of fourth and sixth order are

$$\begin{aligned}
\hat{O}_4^0 &= 35\hat{J}_z^4 - \left[30\hat{J}(\hat{J}+1) - 25\right]\hat{J}_z^2 - 6J(\hat{J}+1) + 3\hat{J}^2(\hat{J}+1)^2 \\
\hat{O}_4^4 &= 0.5(\hat{J}_+^4 + \hat{J}_-^4) \\
\hat{O}_6^0 &= 231\hat{J}_z^6 - 105\left[3\hat{J}(\hat{J}+1) - 7\right]\hat{J}_z^4 \\
&\quad + \left[105\hat{J}^2(\hat{J}+1) - 525\hat{J}(\hat{J}+1) + 294\right]\hat{J}_z^2 \\
&\quad - 5\hat{J}^3(\hat{J}+1)^3 + 40\hat{J}^2(\hat{J}+1)^2 - 60\hat{J}(\hat{J}+1) \\
\hat{O}_6^4 &= 0.25\left[11\hat{J}_z^2 - \hat{J}(\hat{J}+1) - 38\right](\hat{J}_+^4 + \hat{J}_-^4) \\
&\quad + 0.25\left[11\hat{J}_z^2 - \hat{J}(\hat{J}+1) - 38\right](\hat{J}_+^4 + \hat{J}_-^4)
\end{aligned} \tag{4.7}$$

with $\hat{J}$, $\hat{J}_z$ as the usual quantum mechanical operators for the total electronic angular momentum and $\hat{J}_+$, $\hat{J}_-$ the corresponding ladder operators defined as

$$\hat{J}_+ = \hat{J}_{\mathrm{x}} + i\hat{J}_{\mathrm{y}} \tag{4.8a}$$

$$\hat{J}_- = \hat{J}_{\mathrm{x}} - i\hat{J}_{\mathrm{y}} \tag{4.8b}$$

The coefficients $F(4)$ and $F(6)$ are J-dependent and are given for $J = 8$, e.g. in [Ste51] as $F(4) = 60$ and $F(6) = 13860$. The parameters W and x determine the energy scale of the crystal field splitting, where x is defined to be $x \in [-1, 1]$. They are dependent on the detailed nature of the magnetic ionic wave function and highly complicated to derive from theory. The determination of the precise values for W and x therefore requires experimental input. The available parameter space for W and x in Au:Ho is constrained by previous theoretical [Ble89] and experimental [Mur70] investigations. The results obtained by the two groups give conflicting values of $W = -0.112$, $x = -0.357$ [Mur70] and $W = -0.113$, $x = -0.576$ [Ble89]. Both of these parameter sets will be considered in the following discussion.

4.3.2 Numerical calculation of thermodynamic properties

The values of W and x can be determined through measurement of thermodynamic properties, such as heat capacity and magnetisation. For the empirical determination of W and x, it is therefore useful to know their influence on these properties. For this purpose, heat capacity and magnetisation are calculated including only crystal field and magnetic field.

The basis for a thermodynamic calculation of any thermodynamic system is given by the choice of the appropriate thermodynamic potential. In this case, the free energy F is the ideal candidate, with the total differential of

$$dF = -SdT - VMdB \tag{4.9}$$

where the influence of a volume change is already neglected. In statistical physics, this potential can be expressed as

$$F = -Nk_{\mathrm{B}}T\ln z \tag{4.10}$$

where the free energy is a function of the number of magnetic moments N, the Boltzmann constant $k_{\mathrm{B}} = 1.381 \times 10^{-23}\,\mathrm{J/K}$, the temperature T and the single-particle partition function z associated with each magnetic moment

$$z = \sum_i e^{-\frac{E_i}{k_{\mathrm{B}}T}} \tag{4.11}$$

where E_i are the energy levels available to one magnetic moment. The heat capacity C and magnetisation M then follow from equations (4.9)-(4.11):

$$C = \frac{N}{k_B T^2}\left[\langle E^2\rangle - \langle E\rangle^2\right] \tag{4.12}$$

$$M = -\frac{N}{V}\left\langle \frac{\partial E}{\partial B}\right\rangle \tag{4.13}$$

This general theory for magnetic moments shall now be applied to Ho^{3+}-ions in gold. To solve equations (4.12) and (4.13), the energy levels available to the Ho^{3+}-ions at a given temperature must be known. These are essentially obtained by the eigenvalue problem

$$H\,|\Psi_i\rangle = E_i\,|\Psi_i\rangle \tag{4.14}$$

with the Hamiltonian given by

$$H = H_{\mathrm{cf}} + H_{\mathrm{Z}} \tag{4.15}$$

and the eigenstates $|\Psi_i\rangle$. As both the crystal field term H_{cf} and the Zeeman term H_{Z} only include total angular momentum operators, we can chose the 17 states $|J = 8, m_{\mathrm{J}}\rangle$, as a basis. The solution to this eigenvalue problem is then given by diagonalizing the 17×17 matrix spanned by the possible values of m_{J}. Off-diagonal elements in this matrix are introduced by the ladder operators in the Hamiltonian (see equation 4.7).

The exact form of the Zeeman term must still be considered prior to the calculation, as the sensor material is poly crystalline and therefore the crystal field in a given crystallite has an arbitrary orientation with respect to the external magnetic field. In the mathematical description here we follow the opposite approach and assume the coordinate system to be given by the crystal axes and the magnetic field having an arbitrary direction, $\boldsymbol{B} = (B_{\mathrm{x}}, B_{\mathrm{y}}, B_{\mathrm{z}})$, in this coordinate system. Applying this to equation (4.4) results in

$$H_{\mathrm{Z}} = g_{\mathrm{J}}\mu_{\mathrm{B}}|\boldsymbol{B}|\left[\hat{J}_{\mathrm{z}}\cos\theta + \tfrac{1}{2}\hat{J}_{+}(\sin\theta\cos\phi + i\sin\theta\sin\phi)\right] + \tfrac{1}{2}\hat{J}_{-}(\sin\theta\cos\phi - i\sin\theta\sin\phi) \tag{4.16}$$

where θ and ϕ are the usual angles for spherical coordinates. For $\boldsymbol{B} \nparallel \hat{e}_{\mathrm{z}}$, additional off-diagonal terms are introduced in the Hamiltonian. The Au:Ho used during the work for this thesis is generally polycrystalline, the coordinate system given by the crystal field is therefore only valid locally around single Ho^{3+}-ions. To generalise the calculation to the complete ensemble, the thermodynamic properties for different sets of θ and ϕ are averaged. In the following discussion of results, all values are assumed to be averaged without further mention.

The eigenvalue problem and the subsequent calculation of the heat capacity and magnetisation are solved numerically, using Mathematica[1]. The resulting energy eigenstates at zero-field for four sets of crystal field parameters are shown in table 4.1, with different sets of W and x identified by Roman numerals I-IV to simplify the discussion.

[1] Wolfram Research, Inc., Mathematica, Version 8.0, Champaign, IL (2010)

I		II		III		IV	
	E [K]		E [K]		E [K]		E [K]
Γ_5	56.9	Γ_1	54.7	Γ_5	30.5	Γ_1	29.0
Γ_1	48.0	Γ_4	50.3	Γ_1	25.7	Γ_4	26.7
Γ_4	46.5	Γ_3	46.6	Γ_4	24.9	Γ_3	24.8
Γ_3	45.1	Γ_5	44.3	Γ_3	24.1	Γ_5	23.5
Γ_5	7.70	Γ_4	3.57	Γ_5	4.13	Γ_4	1.89
Γ_4	0.14	Γ_3	0.83	Γ_4	0.07	Γ_3	0.44
Γ_3	0.00	Γ_5	0.00	Γ_3	0.00	Γ_5	0.00

Table 4.1: Energy levels for multiplets Γ_i at $B = 0$ for several sets of crystal field parameters. Parameters are given as follows: (I) $W = -0.112$, $x = -0.357$; (II) $W = -0.113$, $x = -0.576$; (III) $W = -0.06$, $x = -0.357$; (IV) $W = -0.06$, $x = -0.576$

The 17-fold degenerated ground state is split into several multiplets Γ_i, which correspond to irreducible representations according to group theory [Abr70]. Since these representations are a result of the natural symmetries of holmium in gold, they are equal for all possible crystal field parameters W and x and consist of 3 low-energy multiplets and 4 high-energy multiplets (see figure 4.2). However, the order of these multiplets ans the qualitative arrangement of mutual energy splitting strongly depends on the parameter x, e.g.for $x = -0.357$ the ground state and first excited state are a Γ_3-doublet and Γ_4-triplet respectively with an energy difference of $\Delta E_{01} = 0.14\,\mathrm{K}$ (parameter set I), while $x = -0.576$ results in a Γ_5-triplet ground state with the Γ_3-doublet as first excited state and $\Delta E_{01} = 0.83\,\mathrm{K}$ (parameter set II). Changing the value of W on the other hand does not change the relative order of multiplets and only scales the magnitude of the energy differences.

The total angular momentum $J = 8$ makes the Ho^{3+}one of two non-Kramers rare earth ions (the other being Tb^{3+} with $J = 6$), which means that the Kramers degeneracy is broken. The Kramers degeneracy signifies, that states must have a multiplicity of at least 2 for $B = 0$ [Abr70], which is lifted linearly by an external magnetic field, i.e. $\Delta E_i = \tilde{\mu}_i B$. Breaking this degeneracy leads to a non-magnetic ground state, visible in figure 4.2. The expected linear dependence of the energy E on the applied magnetic field B (see section 4.2) is only given at large magnetic fields, where the Zeeman effect starts to dominate over the crystal field splitting.

The non-Kramers states are in principle also susceptible to small variations in the crystal field symmetry, due to lattice imperfections, which can lead to a energy splitting of the ground state at $B = 0$. Due to the perfect symmetry assumed in the calculations, this can not be observed in these results.

Figure 4.3 shows the calculated heat capacity and magnetisation for the crystal field

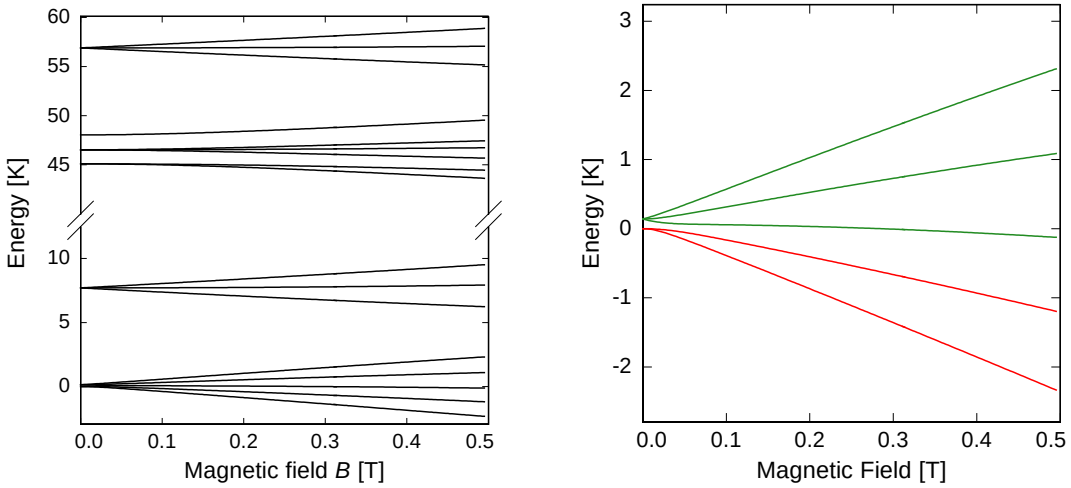

Figure 4.2: Energy levels for crystal field parameter set I (see table 4.1) as a function of magnetic field(left). Ground state multiplet (red) and first excited state multiplet (green) as function of magnetic field B (right).

parameter sets I and II as function of temperature T and inverse temperature $1/T$ respectively.

The magnetisation is given for gold with a concentration of Ho^{3+}-ions of 1 % and an external magnetic field of $B = 0.1\,\mathrm{T}$. It shows the expected Curie-behaviour of a paramagnetic material, with a linear dependence on $1/T$ at high temperatures and a saturation at very low temperatures. Different crystal field parameters result in different slopes at high temperatures and change the saturation magnetisation of the material.

The heat capacity curve shows the contribution of a single implanted Ho^{3+}-ion in the gold matrix. Both sets crystal field parameters result in multiple Schottky anomalies in the heat capacity between 10 mK and 300 K. The ground- and first excited multiplet can be regarded as a two-level system with energy difference $E = E_{01}$ for thermal energies $k_\mathrm{B}T < E$. Neglecting the multiplicitiy of the two levels of this specific two level system, which leads to a factor of order 1, the heat capacity is given by

$$C_S \approxeq N k_\mathrm{B} \left(\frac{E}{k_\mathrm{B}T}\right)^2 \frac{e^{E/k_\mathrm{B}T}}{(e^{E/k_\mathrm{B}T}+1)^2} \tag{4.17}$$

which shows a maximum around thermal energies $k_\mathrm{B}T \approx E/2$. In the case of parameter set I, the lowest Schottky peak is found at $T \approx 70\,\mathrm{mK} \approx \Delta E_{01}/2$, which is in accordance with this model. This curve can be generalized to multiple energy levels, with maxima located at thermal energies between energy levels. The amplitude of the peak depends on the multiplicity of energy levels.

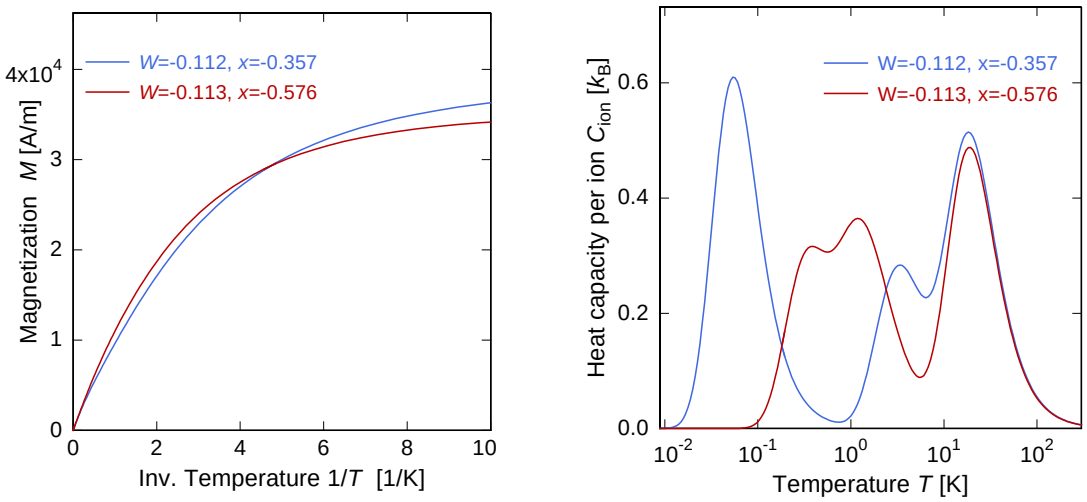

Figure 4.3: Heat capacity C as function of temperature T at $B = 0\,\mathrm{K}$ (right) and magnetisation as function of magnetic field B (left) for $W = -0.112$, $x = -0.357$ and $W = -0.113$, $x = -0.576$

Since the position of the Schottky peaks depends on the distribution of the energy eigenstates, they are highly dependent on the crystal field parameters. For the ECHo experiment the temperature range below 100 mK is of particular interest. At these temperatures the specific heat, is highly influenced by the crystal field parameter x and can show a Schottky peak of significant magnitude.

4.4 Hyperfine interaction

4.4.1 Hyperfine interaction Hamiltonian

The nucleus of the isotope ^{163}Ho has a non-zero nuclear spin of $I = 7/2$, with an associated magnetic dipole moment of

$$\boldsymbol{\mu}_\mathrm{I} = g_\mathrm{I}\mu_\mathrm{N}\boldsymbol{I} \tag{4.18}$$

with the nuclear g-factor $g_I = 1.2$ and the nuclear magneton $\mu_\mathrm{N} = 5.051 \times 10^{-27}\,\mathrm{J/T}$. The interaction of this nuclear magnetic moment with the electronic magnetic moment is described by the hyperfine interaction

$$H_\mathrm{HFI} = hA\boldsymbol{I}\cdot\boldsymbol{J} = hA\left[\hat{J}_\mathrm{z}\hat{I}_\mathrm{z} + \tfrac{1}{2}(\hat{J}_+\hat{I}_- + \hat{J}_-\hat{I}_+)\right] \tag{4.19}$$

where $h = 6.626 \times 10^{-34}\,\mathrm{Js}$ is Planck's constant, A is the hyperfine coupling given as a frequency and $\hat{I}_z$,$\hat{I}_+$,$\hat{I}_-$ are the nuclear spin operators. The basis for the nuclear

spin operators is given by $|I, m_\mathrm{I}\rangle$. The hyperfine coupling A is a material dependent parameter, and its exact value to be determined by experiment. The energy scale of the hyperfine interaction can be of the order of 100 mK, which is comparable to the energy of the first excited state in the crystal field. The hyperfine interaction can therefore not be treated as a perturbation and the energy eigenstates for the combined Hamiltonian

$$H_\mathrm{tot} = H_\mathrm{cf} + H_\mathrm{Z} + H_\mathrm{hfi} \tag{4.20}$$

must be considered instead. The solution of this Hamiltonian and the subsequent calculation of thermodynamic properties follows the principle introduced in section 4.3.2.

Since the combined Hamiltonian H_tot contains both electronic angular momentum operators $\hat{J}$ and nuclear spin operators $\hat{I}$, we now chose as basis the states

$$|J = 8, m_\mathrm{J}\rangle \otimes |I = 7/2, m_\mathrm{I}\rangle = |J = 8, m_\mathrm{J}; I = 7/2, m_\mathrm{I}\rangle \tag{4.21}$$

which are the tensor product of the bases for the electronic angular momentum and the nuclear spin. With the multiplicities of 17 for m_J and 8 for m_I, this results in a 136×136 matrix, which has to be diagonalised.

In principle, the nuclear spin also interacts with the external magnetic field, resulting in an additional Zeeman term

$$H_\mathrm{Z,N} = -g_\mathrm{I}\mu_\mathrm{N}\boldsymbol{B}\cdot\boldsymbol{I} \tag{4.22}$$

However, this effect is suppressed by a factor of $\mu_\mathrm{B}/\mu_\mathrm{N} \approx 2000$ compared to the electronic Zeeman term (equation 4.4). Since the resulting energy scale of this Hamiltonian is significantly smaller than all previously discussed contributions, it will be neglected in the following discussion.

4.4.2 Numerical results

For the hyperfine interaction coupling of Ho^{3+}we find in the literature values of about $A = 812\,\mathrm{MHz}$ [Abr70]. These values were determined for host materials different from gold, which therefore also have different crystal fields. While the effect of the crystal field on the magnetic hyperfine interaction should be negligibly small, a possible deviation from $A = 812\,\mathrm{MHz}$ can not be fully excluded. The ^{163}Ho nucleus also has an electric quadrupole moment, but as most holmium ions should sit on regular lattice sites of the gold host, there should not be any quadrupolar energy splittings due to the cubic symmetry of the fcc lattice.

To understand the influence of the hyperfine interaction on the thermodynamic properties, results for energy levels, heat capacity and magnetisation with varying values

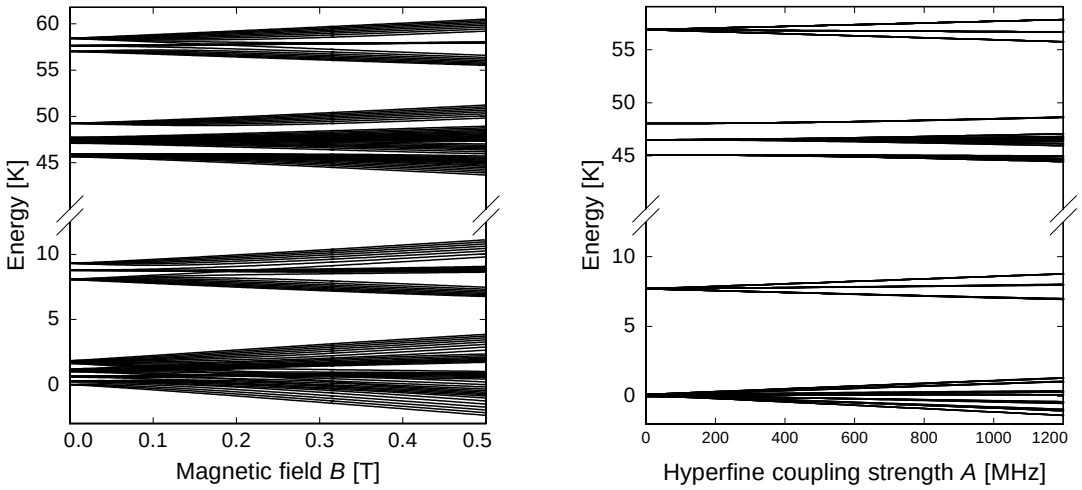

Figure 4.4: Energy levels for crystal field parameter set I (see table 4.1) as a function of the hyperfine coupling strength A (left) and as a function of the magnetic field B for fixed $A = 812\,MHz$.

for A and fixed crystal field are shown in figure 4.4 and 4.5 respectively. The energy level scheme shows the expected rise in the complexity of the energy level system when compared to figure 4.2.

Figure 4.5 (right) shows the magnetisation in a magnetic field of $B = 100\,\mathrm{mT}$. We observe a change in the saturation level at low temperatures, but the magnetisation effectively independent of the hyperfine interaction at temperatures above $T > 1\,\mathrm{K}$. The magnetisation at high temperatures can therefore be fully described by the crystal field, without inclusion of the hyperfine interaction.

The heat capacities shown in figure 4.5 (left) on the other hand are drastically different compared to the pure crystal field case. Only the Schottky peak at low-T has a significant amplitude, with the position given by the energy difference between the ground- and first excited multiplet. As this energy level splitting is caused by the hyperfine interaction, the behaviour of the heat capacity of Ho^{3+}-ions in gold at $T < 100\,\mathrm{mK}$ is dominated by the hyperfine interaction.

4.5 Interacting magnetic moments

The model of Ho^{3+}-ions without mutual interaction, as introduced in the previous sections, provides a qualitative description of the thermodynamic system and is expected to be quantitatively correct at Ho-concentrations $x_{\mathrm{Ho}} \ll 100\,\mathrm{ppm}$. However, for an accurate quantitative calculation at higher concentrations, the interaction be-

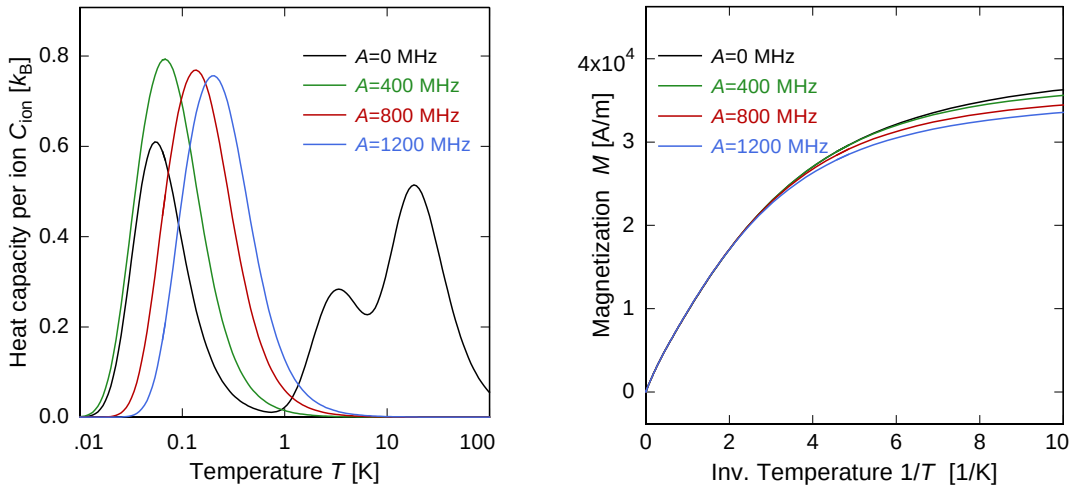

Figure 4.5: Heat capacity C as function of temperature at $B = 0\,\mathrm{T}$ (left) and magnetisation as function of inverse temperature for a magnetic field $B = 100\,\mathrm{mT}$ (right) for different values of the hyperfine coupling strength A.

tween the Ho^{3+}-ions needs to be considered. However, due to the complexity of the energy levels of Ho^{3+}-ions as given in the previous sections, the inclusion of interactions in the calculation exceeds the scope of this thesis.

A brief introduction to the interaction mechanisms and the principle of a solution is given in this section, while a detailed solution for the simpler case of ^{168}Er in gold can be found in the appendix, chapter A.3.

The magnetic dipole-dipole interaction between two magnetic moments $\boldsymbol{\mu}_i$ and $\boldsymbol{\mu}_j$ at respective positions $\boldsymbol{r}_{i,j}$ is given by

$$H_{ij}^{\mathrm{dipole}} = \frac{\boldsymbol{\mu}_0}{4\pi}(g_\mathrm{J}\mu_\mathrm{B})\frac{1}{r_{ij}^3}\left[\boldsymbol{J}_i \cdot \boldsymbol{J}_j - 3(\boldsymbol{J}_i \cdot \hat{\boldsymbol{r}}_{ij})(\boldsymbol{J}_j \cdot \hat{\boldsymbol{r}}_{ij})\right] \tag{4.23}$$

where the relation $\boldsymbol{\mu}_\mathrm{J} = g_\mathrm{J}\mu_\mathrm{B}\boldsymbol{J}$ is used. The distance between magnetic moments is given by r_{ij} and $\hat{\boldsymbol{r}}_{ij}$ denotes the unit vector in direction $\boldsymbol{r}_i - \boldsymbol{r}_i$. The dipole-dipole interaction is anisotropic in nature and decreases in magnitude with r_{ij}^{-3}.

An additional interaction mechanism is caused by the exchange interaction between the localised $4f$-electrons of a single holmium ion and the delocalised electron system of the conduction band, which leads to an indirect exchange interaction between the holmium ions. This mechanism, also called Ruderman-Kittel-Kasuya-Yosida (RKKY) interaction, can be expressed as

$$H_{ij}^{\mathrm{RKKY}} = \mathcal{J}^2\frac{g_\mathrm{J}^2(g_\mathrm{J}-1)^2}{g_\mathrm{J}}\frac{4V_\mathrm{p}^2 m_\mathrm{e}^* k_\mathrm{F}^4}{\hbar^2(2\pi)^3}(\boldsymbol{J}_\mathrm{i} \cdot \boldsymbol{J}_j)F(k_\mathrm{F}r_{ij}) \tag{4.24}$$

with the volume of the primitive unit cell V_p, the effective mass of the free electrons m_e^*, the Fermi wave vector of the gold conduction electrons $k_\mathrm{F} = 1.2 \times 10^{10}\,\mathrm{m}^{-1}$, the Kittel function

$$F(\rho) = \rho^{-3}\left(\cos\rho - \frac{1}{\rho}\sin\rho\right), \tag{4.25}$$

and the parameter $\mathcal{J}$ describing the strength of the exchange interaction between $4f$-electrons and the conduction band [Fle98]. Due to the Kittel function, the RKKY-interaction oscillates between ferromagnetic and anti-ferromagnetic behaviour as a function of distance between Ho-ions. The amplitude of the interaction decreases with the same factor as the dipole-dipole interaction with r_{ij}^3.

Calculations for the system of Au:Er [Fle03][Sch00] showed that a quantum mechanically correct description of these interactions requires a Monte-Carlo simulation for a random distribution of n magnetic moments on a discrete lattice with a combined Hamiltonian of all n magnetic moments. Accurate simulations require about $n = 10$ magnetic moments. For Au:Er at low temperatures $T < 1\,\mathrm{K}$, the single Er-ion can be reduced to a well defined two-level system with spin $\tilde{S} = 1/2$, which results in a Hamiltonian-matrix of size $2^n \times 2^n$ (see appendix chapter A.4).

This reduction is not possible for the Ho^{3+}-ion in gold, due to the small energy gap to the first excited states. Instead, the full Hamiltonian of equation 4.20 needs to be considered with 136 possible spin configurations for a single ion. The resulting Hamiltonian for $n = 10$ interacting spins then spans a $136^n \times 136^n$-matrix, with $136^{10} \approx 2 \times 10^{21}$. The numerical diagonalisation of such a matrix is not feasible with the available computing power.

In the case of Au:Er with several hundred ppm of erbium, interactions between ions lead to a smeared out Schottky anomaly for the heat capacity, which has a reduced amplitude, but is wider than expected for non-interacting ions [Fle03]. The position of the maximum is only sightly changed however. This can be explained by randomly distributed shifts in the lower energy levels, centered around the values for single ions, caused by the random distribution of ions in the lattice.

At such low concentrations no drastic deviation from this behaviour is expected in Au:Ho. The calculations for the non-interacting magnetic moment given in previous sections should provide a good qualitative approximation for the heat capacity at low temperatures.

4.6 Experimental determination of material dependent parameters

The crystal field parameters W and x are material dependent parameters and are best determined experimentally. The same holds to a lesser extent for the hyperfine coupling strength, as theoretical calculations are more reliable for this case. The previous sections showed, that the thermodynamic properties show a clear dependence on these parameters. In the context of this thesis, measurements of the thermodynamic properties of Au:Ho were used to probe these parameters. As the radioactive isotope ^{163}Ho does not exist in nature and has to be produced artificially [Gas14], the naturally occuring and stable ^{165}Ho was used for this purpose. This substitution is possible as both isotopes have the same nuclear spin of $I = 7/2$ and total angular momentum $J = 8$, and therefore show the same behaviour in the theory described in sections 4.3.1 and 4.4.1.

4.6.1 Magnetisation

The results of the calculations shown in section 4.4.2 showed that the magnetisation of Au:Ho does not depend on the hyperfine coupling strength at temperatures above $T > 1\,\mathrm{K}$, while it is dependent on the crystal field parameters at these temperatures. A measurement of the magnetisation in this high temperature range can therefore be used to probe the crystal field parameters independent from the hyperfine interaction.

Magnetisation measurements were performed on a Au:Ho sample with 1 % ^{165}Ho concentration and a mass of $m = 15.3\,\mathrm{mg}$. A commercial MPMS XL5 magnetometer[2] was used, which covers a temperature range $400\,\mathrm{K} > T > 2\,\mathrm{K}$ with a liquid helium based cooling system. The results for measurements at $B = 0.05\,\mathrm{T}$ and $B = 0.1\,\mathrm{T}$ are shown in figure 4.6.

Gold is a diamagnetic material with a magnetic susceptibility of $\chi_{\mathrm{Au}} = -3.45 \times 10^{-5}$, which is independent of temperature and therefore results in an offset in the magnetisation curve. At $T < 50K$, the magnetisation is dominated by the paramagnetic response of the Ho-ions. The crystal field parameters can be extracted by fitting the theoretical curve to the data set.

The resulting best fit is given for $W = -0.112$ and $x = -0.357$, which is in accordance with the result given by [Mur70].

[2] by Quantum Design Inc., 6325 Lusk Boulevard, San Diego, CA 92121-3733, USA URL https://www.qdusa.com

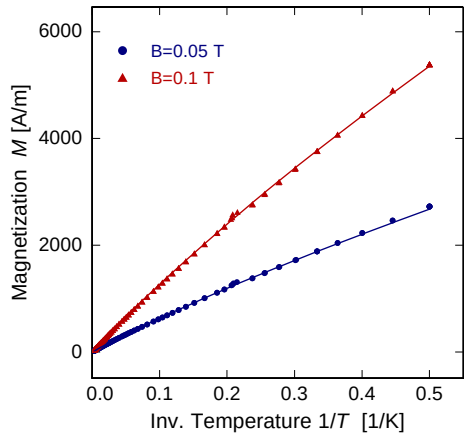

Figure 4.6: Measured magnetisation of $Au_{99}Ho_1$ for $B = 0.05\,T$ and $B = 0.1\,T$, with lines showing a theoretical fit with $W = -0.112$ and $x = -0.357$.

4.6.2 Heat capacity

With the crystal field parameters fixed, numerical calculations using the value of the hyperfine coupling strength $A = 812\,MHz$ found in literature can be used as basis of comparison for measurements of the heat capacity of dilute Au:Ho . At low temperatures the Schottky anomaly was found to be dependent on A. A detailed analysis of heat capacity measurements at $T \approx 100\,mK$ can therefore be used to probe deviations from the literature value of A due to the implantation in the gold lattice. For concentrations above the limit of the dilute alloy, the mutual interactions of the magnetic moments need to be considered for a quantitatively correct description.

The experimental setup for the heat capacity measurement on a metallic magnetic calorimeter with $N_{Ho} = 9 \times 10^{13}$ implanted holmium ions, which was carried out during this work, is described in the following chapter. The analysis of the experimental results is presented in chapter 6 and compared to the numerical results of the theory.

5. Experimental methods

5.1 Cryostat

As described in chapter 3, magnetic calorimeters are operated at temperatures below 100 mK. Several different methods are viable to achieve these low temperatures [Ens05]. In the context of this thesis, an adiabatic demagnetisation refrigeration cryostat (ADR[1]) was used. A detailed description of an ADR-cryostat's cooling principle is given in [Ens05]. The specific features of the cryostat used for the experiment, shown in figure 5.1, will be introduced in the following.

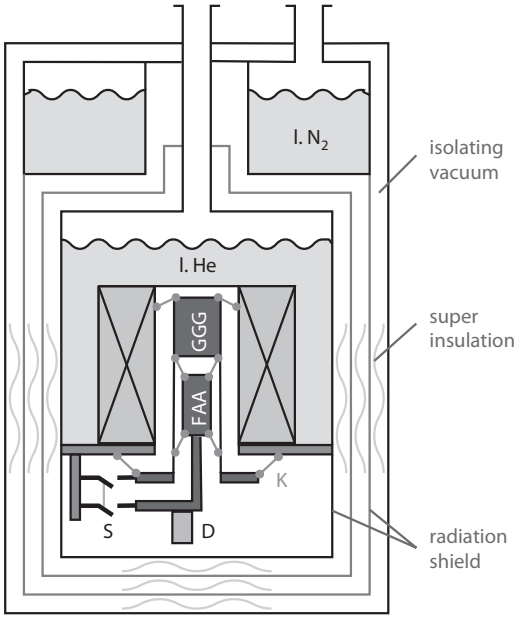

Figure 5.1: Schematic cross section of the ADR-cryostat. The paramagnetic FAA- and GGG-pills are fixed with Kevlar-threads (K) and can be thermally coupled to the 4 K-platform with a mechanical heat-switch (S). The experimental platform (D), is in good thermal contact with the FAA-pill.

The cryostat consists of multiple nested containers, which act as temperature shields with decreasing temperature, going from the outer shield at room temperature to the innermost shield at the temperature of the helium bath. The outer stage is vacuum sealed so the inside of the cryostat can be kept at a typical operating pressure of 10^7 mbar to prevent convective heat exchange. The outer stage is followed by two intermediate shields: The first one is thermally coupled to a bath containing liquid N_2 at 77 K with the second one connected to the outlet of the liquid He bath at a temperature of about 23 K. Then follows the inner stage with the so-called 4K-platform, which is cooled with liquid helium to 4.2 K. By reducing the vapour pressure

[1] **A**diabatic **D**emagnetization **R**efrigerator; B04, CSP/Vericold GmbH, Ismaning (currently Oxford Instruments)

of the helium bath, the temperature of the inner shield can be reduced to around 1.5 K. Superisolation consisting of aluminum foil is located between all of these shield,

In the centre of the cryostat are two paramagnetic salt pills made of GGG[2] and FAA[3]. The GGG-pill is fixed to the 4K-platform using kevlar threads with low heat conductance. Due to its high concentration of magnetic moments, the GGG-pill has a large heat capacity. It serves as a heat sink to prevent parasitic heat flow to the FAA-pill, to which it is attached with kevlar threads. The FAA-pill is then connected via a copper rod to the experimental platform, where the detectors and SQUID-magnetometers used in this thesis were attached. All wires connected to the experimental platform were thermally coupled to all of the previously described heat shields, in particular the thermal connections to 4K-platform and the GGG-pill are very delicate, to reduce the heat flow to the experimental platform.

To create the magnetic field for the adiabatic demagnetisation cooling process, a superconducting magnet is located in the helium bath around the FAA- and GGG-pills. The magnet can carry currents of up to 37 A leading to a maximum field of about 6 T. During the magnetisation of the salt pills a mechanical heat switch provides the thermal connection between the salt pills and the 4K-platform. The switch is opened, when the pills are fully thermalised at maximal magnetic field strength. Reducing the magnetic field when the pills are thermally isolated decreases the temperature of the pills and the attached experiment until the base temperature at zero-field is reached.

For the GGG-pill the base temperature is 250 mK, while the FAA-pill has a lower concentration of magnetic moments and can therefore reach a temperature of 22 mK. As no cooling power is available after full demagnetisation, the pill temperature slowly increases due to radiation and the heat input through finite thermal conductivities of the wires used for the read out of the experiments and thermometers. The time the FAA-pill, and in extension the experiments, stay at the lowest temperature is strongly dependent on these thermal loads. To measure the temperature of the experimental platform a ruthenium oxide resistor[4] was read out with an AVS-47[5] resistance bridge.

As the temperature of the salt pills is dependent on the external magnetic field, the superconducting magnet can be used for temperature stabilization at temperatures above base temperature. For this purpose the temperature signal is fed into a software PID-controller where the required temperature can be set. The output signal

[2]Gadolinium Gallium Garnet: $Gd_3Ga_5O_{12}$

[3]Ferric Ammonium Alum: $Fe_2(SO_4)_3(NH_4)_2SO_4 \cdot 24H_2O$

[4]This thermometer was calibrated at the Walther-Meissner-Institute in Munich and has a relative sensitivity of $\log(R)\ \log(T) = -1.5$ in the temperature range from 21 mK to 40 mK

[5]AVS-47, Pico Watt Elektronika, Finland; relative accuracy: $\Delta R/R = 1 \times 10^{-4}$

then controls the magnitude of the injected current in the magnet, to stabilize the temperature at the set value.

5.2 Detector

The primary goal for the heat capacity measurement of holmium in gold is to define the maximum ^{163}Ho activity, that can be implanted in a single detector without the corresponding heat capacity becoming dominant (see section 2.2.1). A detector having the same design as the prototype described in section 3.5 was used for this thesis. Since this design is optimized for the implantation process, the comparison with available data allows to directly observe any possible impact on the detector performance from the implanted holmium. The information on the contribution to the total heat capacity of the detector is deduced in this thesis by analysing the height of thermal pulses generated by the absorption of a known energy in the detector, according to equation 2.9. In this work, a ^{55}Fe calibration source with $E(k_\alpha) = 5.899\,\mathrm{keV}$ was used. The signal shape was compared to the expected shape without the presence of holmium [Seg09].

A schematic of the detectors used in this work is shown in figure 5.2. The design differs in two aspects from the previously described version shown in figure 3.8: The upper half of the absorber is left out while stems between absorber and sensor have been added.

As the upper absorber half only serves to completely encase the embedded ^{163}Ho source, it is not needed for a measurement of a purely external calibration source. Leaving it out of the design has the advantage of decreasing the heat capacity of the absorber by a factor of two as its total volume is reduced to $(185 \times 185 \times 5)\,\mu\mathrm{m}^3$. This increases the relative contribution of the holmium heat capacity $C_{\mathrm{Ho}}/C_{\mathrm{det}}$. The stems between absorber and sensor are included to avoid loss of athermal phonons, which otherwise could enter the substrate without properly thermalising with the sensor. The additional heat capacity from the stems is less than 1 % of the total detector heat capacity.

5.3 Implantation at RISIKO

Three chips were prepared for implantation with different amounts of the stable ^{165}Ho , $N_1 = 9 \times 10^{12}$, $N_2 = 9 \times 10^{13}$ and $N_3 = 9 \times 10^{14}$ with an uncertainty in the implantation process of 10 %. These amounts correspond to ^{163}Ho -activities of $A \approx 4\,\mathrm{Bq}$, $A \approx 40\,\mathrm{Bq}$ and $A \approx 400\,\mathrm{Bq}$, which is in the order of the activity limit set by the unresolved pile-up fraction given in section 2.2.1.

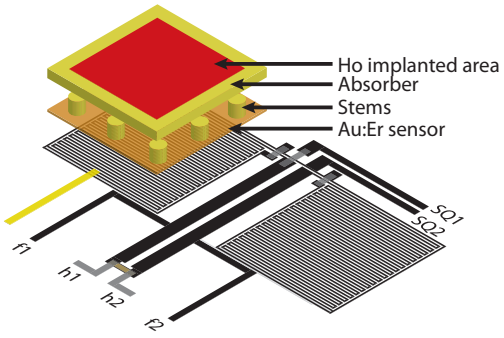

Figure 5.2: Schematic of one pixel in the detector.

The chip was glued to a glass plate and a layer of photoresist was used to restrict the area of implantation to a 160 μm $\times$160 μm area. A 100 nm thick layer of gold is then deposited on top of the whole chip and the glass plate, which made it possible to measure the ion current during the implantation process by attaching an electrode to the gold covering the glass plate.

The photoresist, along with the gold on top of it, is removed after the implantation process. The deposited gold on top of the absorbers adds a volume of $(160 \times 160 \times 0.1)\,\mu\text{m}^3$ to the absorber with heat capacity of about 1 % of the whole absorber.

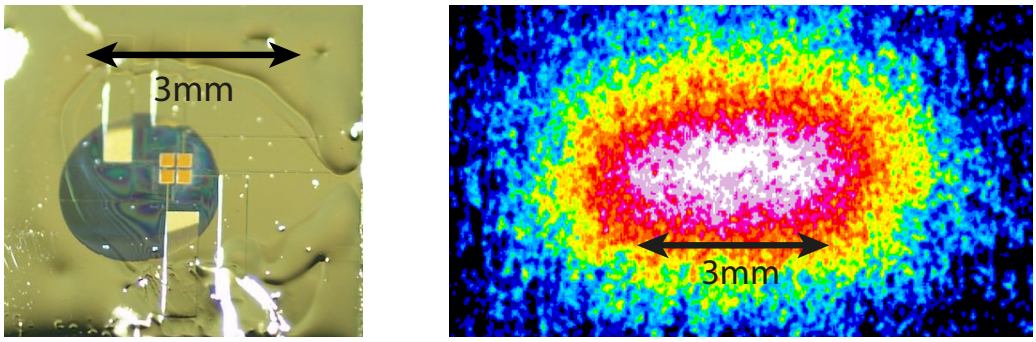

Figure 5.3: Chip after the implantation with highly visible area of implantation on the conductive gold layer (left). Measured beam profile on the target area using autoradiography (right), with increasing intensity from black to white.

The implantation was carried out at the RISIKO mass spectrometer at the Mainz University [Wen99].

The holmium target for the production of the ion beam consists of holmium nitrate onto a titanium foil. The foil is rolled and inserted into a tungsten holder which can be heated to about 2000 °C. Holmium atoms are created by sublimation and a laser is then used for resonant ionisation. The ions are accelerated to 30 keV by applying a high negative voltage along the beam-line. A mass spectrometer is then used to create a pure ^{165}Ho beam. The mass spectrometer is made of a magnetic dipole, which deflects the ions at an angle depending on their mass and the magnitude of

the applied magnetic field. By tuning the magnetic field, ions with the mass of ^{165}Ho can be selected to hit a fixed target area, where the chip is positioned. A magnetic lens system in front of the chip is used to focus the beam on a small area.

Figure 5.3 shows the profile of the implantation area. The profile was determined using autoradiographic imaging. For that purpose a titanium foil implanted with ^{165}Ho which was irradiated with neutrons, creating the isotope ^{166}Ho which can be recorded with gamma detectors.

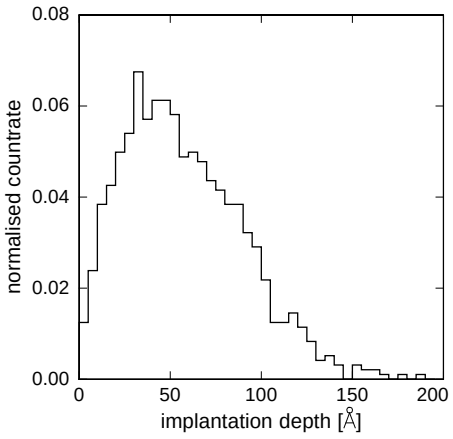

Figure 5.4: Implantation depth profile in Au for ^{165}Ho ions with 30keV energy, calculated with SRIM.

This RISIKO facility achieves a mass separation of $m/\Delta m \approx 500$, which is more than sufficient to suppress any source contaminations during implantation. SRIM[6] calculations for the ion-energy of 30 keV result in the implantation depth profile shown in figure 5.4, with an average implantation depth of 55 below the absorber surface.

Figure 5.5 shows the absorber surface of the three chips after the implantation process. For the chips with higher concentration, a change in the surface colour of the implantation area is clearly visible, while the chip with the lowest concentration is mostly unchanged. Calculations for the holmium concentration show, that while the assumption of a dilute Au:Ho alloy holds for the chip with the lowest amount of holmium, this is not the case for the other two chips with concentrations exceeding the 10 % level. Using an implantation depth of $d = 10\,\text{nm}$ and implantation area of $160 \times 160\,\mu\text{m}^2$ in the gold absorber, the fraction of Ho-ions to Au-ions of

$$\frac{N_{\text{Ho}}}{N_{\text{Au}}} = 5.95 \tag{5.1}$$

is found for $N_{\text{Ho}} = 9 \times 10^{13}$. This means, that the surface of high concentration chip should be modeled to have a layer of pure holmium deposited on top of the gold

[6]The Stopping and Range of Ions in Matter, licence free software, www.srim.org

absorber, with a gradient in holmium concentration between 0 % and 100 % in the first 10 nm of the gold absorber.

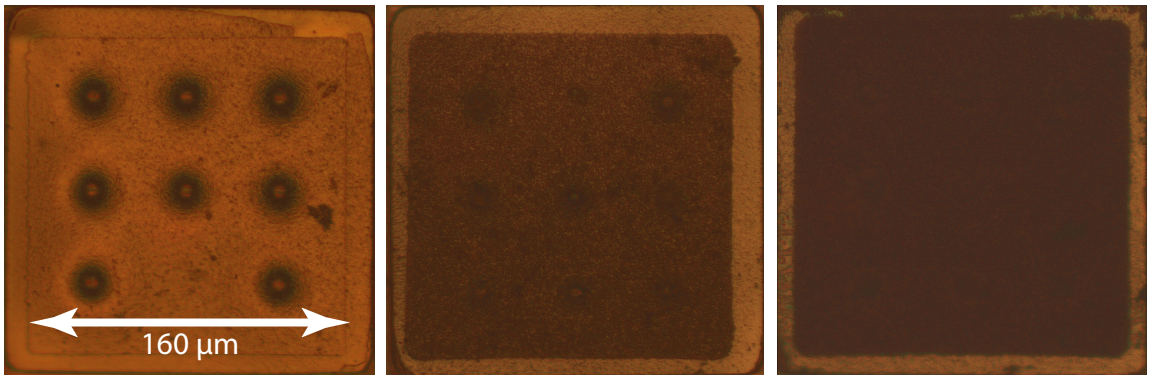

Figure 5.5: Absorber surface for each of the three implanted chips after implantation at RISIKO. Increasing Ho-abundancy from left to right: $N_{\mathrm{Ho}} = 9 \times 10^{11}$, $N_{\mathrm{Ho}} = 9 \times 10^{12}$, $N_{\mathrm{Ho}} = 9 \times 10^{13}$

5.4 Experimental setup

After the implantation process, the protective photoresist layer was removed together with the conductive gold layer. The two chips with higher holmium concentration have been installed in a dedicated experimental setup. During this thesis only the detector with the highest concentration was fully characterised. The detector holder this chip was glued to was made out of oxygen free copper and is characterized by a small island where the detector chip and the read out SQUIDs are glued [Ran14]. The SQUIDs for the readout used a 2-stage configuration as described in section 3.4, where the front-end SQUID and the amplifier SQUID array were fabricated on the same chip. The chips were produced by the PTB[7] and are called C6X114HW.

The basis of the experimental setup, shown in figure 5.6, is a 18 mm × 80 mm holder made of solid copper ①, with a platform of 23 mm × 16 mm situated in its middle. The chips containing the detectors ② and SQUIDs ③ were glued to the middle of this platform with GE 7031[8] varnish. Two circuit boards ④ and ⑤ are situated around the chips to provide the electrical connections needed for the read-out of the detector. One end of the circuit boards is glued to the elevated platform with Stycast 2850 FT[9], while the other is not fixed, to allow bending due to different thermal expansion

[7]Physikalisch Technische Bundesanstalt , Berlin, Germany

[8]Lake Shore Cryotronics Inc., 575 McCorkle Boulevard, Westerville, OH 43082, USA, www.lakeshore.com.

[9]by Emerson&Cuming, part of Henkel Corporation, 15350 Barranca Parkway, Irvine, CA 92618 USA, URL http://www.henkel.com

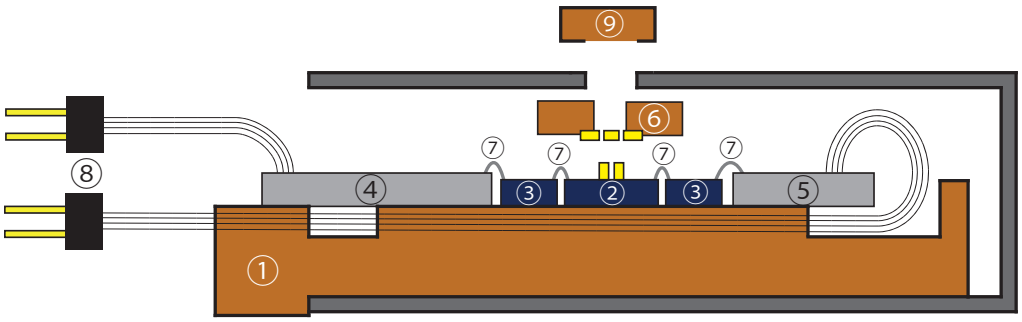

Figure 5.6: Schematic of the experimental setup. See text for full description.

coefficients. The surface of the copper holder around the platform is covered with kapton foil to avoid electrical connections between the electric lines on the backside of the circuit board and the copper holder.

Electrical connections between the chips and the circuit board are made with wedge bonded 25 μm diameter aluminum wires ⑦. The operating temperature, $T < 100\,\mathrm{mK}$, of the experiment is well below the critical temperature of aluminum $T_\mathrm{c} \approx 1.2\,\mathrm{K}$, ensuring superconducting behaviour of these wires. To the other ends of the circuit boards superconducting wires made of NbTi are soldered, which have connectors attached to them ⑧.

Gold wires with 25 μm diameter are wedge bonded from the detector chip and SQUID to large copper areas on the circuit board to increase the contact to the thermal bath.

A collimator ⑥ is used to ensure that x-rays from the ^{55}Fe source ⑨ hit only the detector's absorber. This is fabricated using a 2 mm wide and 1 mm high copper bridge which is glued across the detector chip. The collimator has a hole of 1 mm diameter located above the detectors. To reduce the collimator area, a gold foil of 20 μm thickness is placed, which has two holes of $d \approx 80\,\mu\mathrm{m}$ diameter placed 200 μm apart. These holes are aligned with two of the absorbers.

The whole experimental setup is surrounded by a lead shield, to shield from time-varying magnetic field. It is made of 1 mm thick lead, which has a welded edge. The shield is superconducting below $T_\mathrm{c} \approx 7.2\,\mathrm{K}$. For an optimal shielding effect, the opening to allow for wiring connections is placed at a large distance from the detector and SQUID. To allow x-rays from the external calibration source to hit the detector, an additional hole of $d \leq 3\,\mathrm{mm}$ diameter is drilled above the previously described collimator.

5.5 ^{55}Fe X-ray calibration source

To obtain the heat capacity in a calorimetric measurement, the event energy E has to be known. In the experiment discussed in this thesis, an external ^{55}Fe x-ray source was used for that purpose. ^{55}Fe decays via electron capture to ^{55}Mn with a half-life of $T_{1/2} = 2.73\,\mathrm{y}$ with subsequent emission of x-rays and electrons from the excited daughter atom ^{55}Mn. The dominant x-ray energies, with relative amplitudes of 9 to 1, are 5.895 keV for the K_α-line (transition from the L-shell to the K-shell) and 6.490 keV for the K_β-line (transition from the M-shell to the K-shell). Both the K_α- and K_β-line show fine structure splitting due to transitions from sub-levels of the L- and M-shells, which can be resolved with high energy resolution detectors.

The source is encased in such a way, that auger electrons and x-rays from lower energy transitions are stopped with $p \approx 100\,\%$. Therefore, only the dominant K_α and K_β x-rays can leave the source and hit the detector, which ensure a well defined x-ray energy.[10]

At the time of the experiment, the ^{55}Fe source had an activity of $A \approx 6.0\,\mathrm{MBq}$. Positioned 2.5 cm away from the detector using a copper arm connected to the 4K-platform, this results in a count rate of 4 Bq on the absorber of the MMC.

5.6 Room temperature electronics and data acquisition

The treatment of the SQUID signal at room temperature is performed using the XXF-1[11] electronic. This SQUID electronics contains the FLL-circuit as described in chapter 3.4 and controls the SQUID. The output voltage signal of the FLL-circuit is proportional to the flux change in the pick-up coil of the MMC. This output signal is split in two paths.

One of the paths is used to read out the DC voltage signal to gain the temperature information of the chip due to magnetisation changes (see section 3.3).

The other path is digitized by a high speed digitiser with 12-bit resolution and is AC coupled to acquire the data corresponding to x-rays hitting the absorber of the calorimeter. The data acquisition and operation of the digitizer is done with a computer program, which is described in detail in [Sch00]. When energy is deposited in the absorber, a pulse-shaped voltage signal is generated. If this signal exceeds a pre-set trigger value, a selectable time-window containing 16384 data points is saved.

[10] Gamma rays from IBEC (Internal Bremsstrahlung in Electron Capture), with an energy spectrum up to 400 keV, can leave the source at rates 10^{-4} lower than the x-ray emission.

[11] by Magnicon GmbH, Barkhausenweg 11, 22339 Hamburg, Germany URL http://www.magnicon.com

The time window is chosen in such a way, that the pulse begins after 25 % of the recorded data and contains the interesting part of the signal. This includes the rise time and the decay of the signal down to 70 % of the maximal height.

6. Experimental results

For the investigation presented in this thesis, three chips were implanted with different concentrations of ^{165}Ho as discussed in chapter 5.3. The measurements discussed here were performed on the chip with the highest amount of ^{165}Ho-ions. An experimental characterisation of the used detector is given in section 6.1.

Pulse-height measurements for different persistent currents and temperatures were carried out to determine the heat capacity of the detector using equation 3.4. The results for these measurements will be analysed in section 6.2.

6.1 Detector characterisation

The accurate analysis of the pulse-height requires the understanding of a number of detector properties. For that purpose, supporting measurements of the SQUID noise and the magnetisation curve of the Au:Er-sensor were carried out, which are discussed in the following.

6.1.1 Flux coupling

The flux coupling between the pick-up coil and the SQUID input coil for the double meander geometry is given by

$$k_\Phi = \frac{\delta\Phi_\mathrm{S}}{\delta\Phi} = \frac{M_\mathrm{is}}{L_m + 2(L_i + L_w)} \tag{6.1}$$

where $\delta\Phi$ is a change of flux in one of the two meanders, $\delta\Phi$ the resulting flux change in the SQUID, M_is is the input sensitivity of the SQUID, L_m is the inductance of a single meander, L_i is the input inductance of the SQUID and L_w the inductance of the aluminum bonding wires between the pick-up coils and the input coil. The value of $k\Phi$ can be determined by characterising the spectral density of the flux noise in the SQUID-magnetometer.

In the temperature range $1.2\,\mathrm{K} < T < 9.25\,\mathrm{K}$, the pick-up coils and the input-coil of SQUID magnetometer are superconducting, while the aluminum wires have a finite resistance R_w. This resistance is a source of white voltage noise, according to the fluctuation-dissipation theorem [Joh28][Nyq28], with a spectral power density of

$$S_\mathrm{U} = \frac{\langle U^2 \rangle}{\Delta f} = 4 k_\mathrm{B} T R_\mathrm{w} \quad . \tag{6.2}$$

The corresponding current noise directly induces a magnetic flux noise in the SQUID which can be described by a low-pass characteristic,

$$S_\Phi(f) = M_{\mathrm{is}}^2 \frac{4k_\mathrm{B}T}{R_\mathrm{w}} \frac{1}{1-\left(\frac{f}{f_0}\right)^2} \tag{6.3}$$

where the cut-off frequency

$$f_0 = \frac{R_\mathrm{w}}{2\pi L_\mathrm{tot}} \tag{6.4}$$

is caused by the RL-circuit formed by the wire resistance R_w and the total inductance of the read-out circuit

$$L_\mathrm{tot} = L_\mathrm{i} + L_\mathrm{w} + \frac{L_\mathrm{m}}{2} \tag{6.5}$$

which is given by the previously defined inductances.

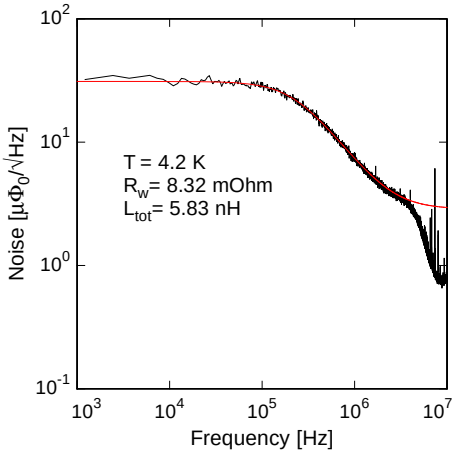

Figure 6.1: Measured spectral flux density in the SQUID at $T = 4.2\,\mathrm{K}$.

Figure 6.1 shows the measured spectral density of magnetic flux noise in the front-end SQUID of the integrated SQUID-magnetometer of type C6X114HW at a temperature of $T = 4.2\,\mathrm{K}$. At frequencies below $f \approx 300\,\mathrm{kHz}$, the plateau and low-pass behaviour of the current noise described by equation 6.3 dominates the spectral density. Above $f \approx 1\,\mathrm{MHz}$ a second plateau is visible, which is caused by the intrinsic white noise of the SQUID and leads to a second low-pass cut-off frequency which is given by the finite bandwidth of the SQUID read-out electronics.

The spectrum can consequently be described by the sum of two low-pass filters

$$S_\Phi(f) = M_{\mathrm{is}}^2 \frac{4k_\mathrm{B}T}{R_\mathrm{w}} \frac{1}{1-\left(\frac{f}{f_0}\right)^2} + S_{\Phi,SQ} \tag{6.6}$$

where $S_{\Phi,\mathrm{SQ}}$ denotes the spectral density of the intrinsic flux noise of the SQUID. Fitting this function to the measured spectral density then results in values of:

$$R_\mathrm{w} = 8.32\,\mathrm{m\Omega} \tag{6.7}$$

$$L_\mathrm{tot} = 5.83\,\mathrm{nH} \quad . \tag{6.8}$$

The inductance of the aluminum wires can be derived using an empirically found relation between inductance and resistance

$$L_\mathrm{w} \approx 0.15\frac{\mathrm{nH}}{\mathrm{m\Omega}} R_\mathrm{w} = 1.25\,\mathrm{nH} \tag{6.9}$$

which should hold in the situation where each bonding pad of the SQUID input coil is connected to the corresponding bonding pad of the detector chip by two aluminum-wires with a diameter of $25\,\mu$m in the normal conducting state. Using (6.5) and the input inductance $L_\mathrm{i} = 1.8\,\mathrm{nH}$ of the SQUID of type C6X114HW results in an inductance of a meander of

$$L_\mathrm{m} = 5.56\,\mathrm{nH} \tag{6.10}$$

which is significantly larger than the simulated value of $L_\mathrm{m} = 2.0\,\mathrm{nH}$. The reason for this deviation, which is also present in previous experiments with this detector design [Ran14] is not yet found. Possible explanations are fabrication imperfections and a simplified detector geometry used in the simulation.

Using equation 6.1, a flux coupling of

$$k_\Phi = 0.033 \tag{6.11}$$

is found for the measured inductance.

6.1.2 Temperature dependent magnetisation of the Au:Er sensor

Since the detector used for the experiment has only one of the two meander shaped pick-up coils of each read-out channel equipped with a sensor, the detector signals are sensitive to the absolute temperature of the substrate. Measuring the SQUID output-voltage as a function of the FAA-pill temperature T_FAA is therefore a direct measure of the sensor's magnetisation $M(T)$.

Figure 6.2 shows the measured magnetic flux in the front-end SQUID for different persistent currents in the loop formed by the two meanders. These datasets are compared to the corresponding numerically calculated curves, which take into account the properties of the detector, including the geometry of the meander and the sensor, the Er-concentration in the sensor, and the magnetic field generated by the injected persistent current. The Er-concentration was determined to be 311 ppm with a magnetisation measurement on residual material of the micro-fabrication process in an

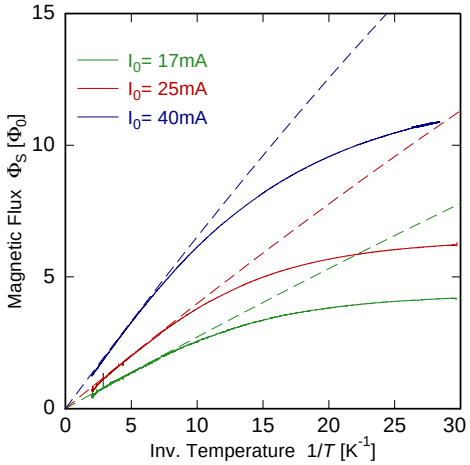

Figure 6.2: Measured magnetisation of the Au:Er sensor as function of temperature T for different persistent currents. The dotted lines denote the expected curve from simulations.

MPMS XL5 magnetometer[1] in the temperature range 2 K to 300 K. This is possible, as the paramagnetic sensors are patterned using a lift-off process.

At temperatures above 100 mK the measured data is proportional to $1/T$ as expected from the Curie law. A clear discrepancy between the measured- and calculated magnetisation is visible at low temperatures. This deviation in the measurement has been seen in a few previous experiments [Ran14] and is a sign for thermal decoupling of the experiment from the FAA-pill temperature, which should be improved in future experiments. The bias currents necessary to operate the two-stage SQUID-magnetometer dissipate power and heat the chips containing the SQUIDs and the detector locally. If the thermal link between the chips and the experimental platform is too weak, the chips can not thermalize properly, leading to an increased temperature relative to the FAA-pill. A reason for this thermal decoupling is the breaking of the glue[2] joint between the detector chip and the chip holder made of copper during the cooldown of the cryostat, due to different thermal expansion coefficients.

The true temperature T_{det} of the detector can be extracted as a function of the FAA-pill temperature T_{FAA}, by projecting the measured values of the magnetisation $M(T_{\mathrm{det}})$ onto the expected, numerically calculated magnetisation curve $M(T_{\mathrm{FAA}})$, represented by dashed lines in figure 6.2.

Different thermal links connect the sensor of the MMC with the experimental platform serving as thermal bath. One channel for thermal transport is due to the electric link through the gold bonds to the copper holder and then the experimental platform. Another is given by the phononic coupling to the substrate, which is connected with the glue joint to the copper holder. If one of these paths dominates in

[1] by Quantum Design Inc., 6325 Lusk Boulevard, San Diego, CA 92121-3733, USA URL https://www.qdusa.com

[2] GE 7031

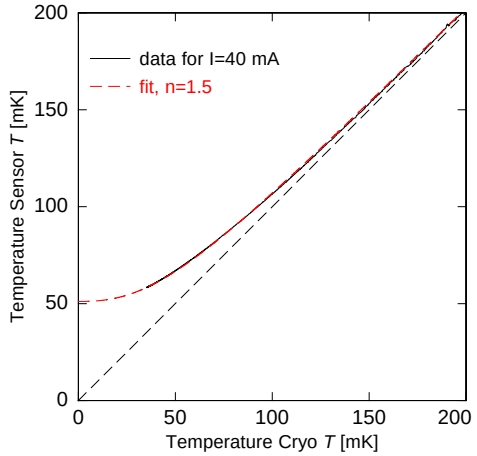

Figure 6.3: The corrected temperature T_{det} as function of the measured temperature T_{FAA} of the experimental platform for the persistent current $I_0 = 25\,\mathrm{mA}$ (solid lines). The dotted line is a guide for the eye representing $T_{\mathrm{det}} = T_{\mathrm{FAA}}$.

this temperature range, the sensor temperature should be well described by

$$T_{\mathrm{det}} = \left(T_{\mathrm{FAA}}^{n+1} + T_0^{n+1}\right)^{1/(n+1)} \tag{6.12}$$

where $n = 1$ for a dominant link made of normal conducting metal or $n = 2$ for a dominant link carried by phonons in an amorphous material like glue. In figure 6.3 the measured data for $I = 40\,\mathrm{mA}$ is shown as a solid black line and a fit of (6.12) with $n = 1.5$ as a dashed red line. This value of n suggests that both of the two thermal links contribute to the thermalisation behaviour of the sensor, but there is no single dominant path for the heat flow. This could be due to a partial disconnect of the chip from the GE 7031 varnish used for the glue joint, which would weaken the phononic connection significantly and could cause the observed thermal decoupling.

6.2 Heat capacity measurement

For the heat capacity measurement, the response of the detector to x-rays of a ^{55}Fe calibration source is analysed. With a known energy input, equation $\Delta T = \Delta E / C_{\mathrm{tot}}$ allows for the determination of the total heat capacity of the detector. If the thermal coupling of the magnetic moments of the erbium ions, which represent the thermometer, to the other degrees of freedom in the detector is good, the signal rise is fast and we can use the initial temperature change $\Delta T(t = 0)$ of the pulse in this relation. For all temperatures and persistent currents, the heat capacity of the Au:Er sensor and the gold absorber can be calculated, and data sets from previous measurements on similar detectors [Seg09] provide a basis of comparison for the signal size observed here. In micro-fabricated MMCs, an additional heat capacity is typically observed which is related to structural defects in the Au:Er and Au layers from the sputtering process. This heat capacity seems to vary with the given sputtering conditions between $2\,\mathrm{JK^{-1}m^{-3}}$ and $10\,\mathrm{JK^{-1}m^{-3}}$, where the highest values

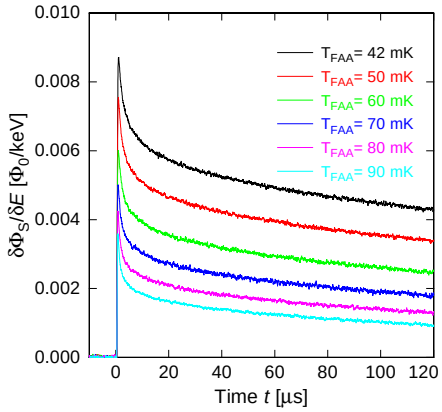

Figure 6.4: First 120 μs of the averaged signals for $I_0 = 40\,\mathrm{mA}$ at different temperatures.

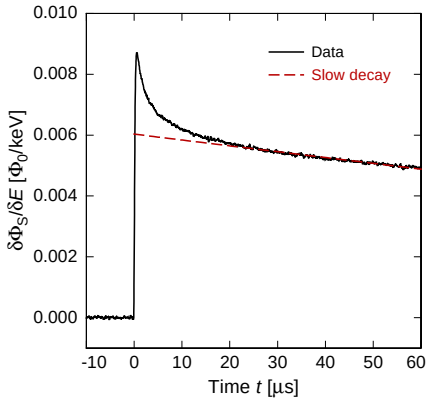

Figure 6.5: First 60 μs of the averaged signal for $I = 40\,\mathrm{mA}$ and $T = 42\,\mathrm{mK}$ shown as black solid line. The secondary slow decay is shown by the dashed red line.

are found for Au:Er and the lowest for sputtered high purity Au [Gas13]. As all other parameters are known in these conditions, the heat capacity of the implanted holmium can be extracted from the analysis of the measured pulse height.

An average over several 100 events corresponding to ^{55}Fe K_α-x-rays with an energy of 5.899 keV was taken at various temperatures between $T_{\mathrm{FAA}} = 40\,\mathrm{mK}$ and $T_{\mathrm{FAA}} = 100\,\mathrm{mK}$ and for three different persistent currents. A time-window of 120 μs was used, where the signal height drops to about 70 % of the maximum height. Figure 6.4 shows the averaged and normalised pulses are for a persistent current of $I_0 = 40\,\mathrm{mA}$ in the meander shaped pick-up coil.

In the simplified thermodynamic description of a magnetic calorimeter in chapter 3.2.1, the pulse shape is described by a fast rise time $\tau_0 \approx 100\,\mathrm{ns}$ resulting from the electron-spin coupling given by the Korringa relation, and a decay time given by the ratio between the total heat capacity and the thermal conductivity to the bath, $\tau_1 \approx C_{\mathrm{tot}}/G_{\mathrm{eb}}$. For real devices, additional features in the pulse shape can be observed, e.g. due to the nuclear electric quadrupole moments of gold. These can introduce an additional heat capacity which causes an additional decay time of 200 μs to 2 ms clearly visible at temperature below 40 mK, but should be negligible in the temperature range of the experiment discussed here.

The signal amplitude and the associated heat capacity of the detector can be obtained by fitting exponential rise and decay functions to the signal shape (see chapter 3.2.1). The rise-time for the measured signals was found to be $\tau < 200\,\mathrm{ns}$, which is about a factor of 2 slower than the intrinsic rise time and limited here by the bandwidth of the read-out scheme. The maximum amplitude after the exponential rise can be

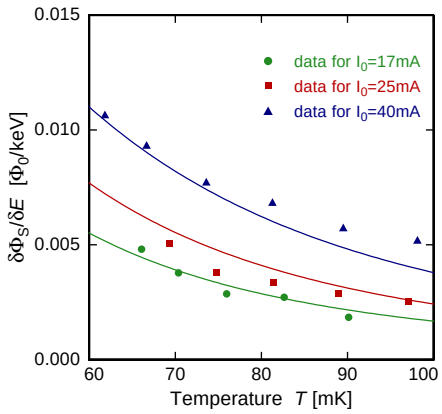

Figure 6.6: Normalised signal heights as function of temperature for different persistent currents. Expected values from simulations of the detector are shown as solid lines.

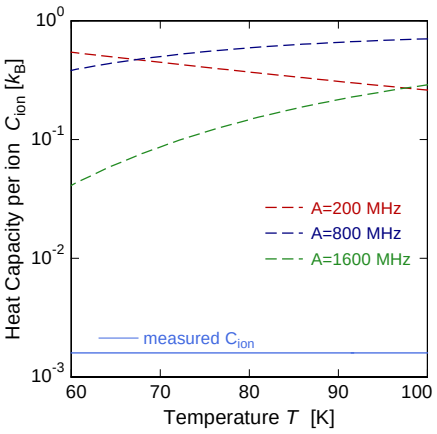

Figure 6.7: Comparison of the heat capacity per implanted ion from measurements (solid line at $1.6 \times 10^{-3}\,\mathrm{pJ/K}$) and numerical calculations for different values of A using $W = -0.112$, $x = -0.357$ as described in chapter 4.6.

compared with one the expected from [Seg09], where an additional heat capacity of $0.5\,\mathrm{pJ/K}$ from the sputtering process was determined for this type of detector. Figure 6.6 shows the measured maximal signal height as a function of temperature in comparison to simulated values for the detector which are in accordance with [Seg09]. There is no evidence for a significant additional heat capacity due to the implanted holmium.

The decay of the signals does not show a simple exponential behaviour, suggesting that the detector consists of more than the thermodynamic systems of absorber (conduction electrons) and temperature sensor (magnetic erbium ions). Instead, the decay of the pulse can be divided into a part with a fast decay time $\tau_1 \approx 10\,\mu\mathrm{s}$ and a second part with a decay time, which is significantly larger than the measured time-window of $\Delta t = 120\,\mu\mathrm{s}$ and can therefore not be determined precisely from the recorded data.

This signal shape suggests that energy deposited by the absorbed x-ray thermalises within the conduction electrons, phonons and the magnetic moments of the erbium ions and then leaks into an additional thermodynamic system on a time scale of a few μs, before finally flowing through the thermal link to the thermal bath formed by the chip holder and the experimental platform. This additional system could be related to the implanted holmium ions. If the heat capacity of the detector is

calculated using the amplitude of the slow decay, an additional heat capacity of

$$C^{\text{add}} \approx 2.0\,\text{pJ/K} \tag{6.13}$$

is found almost independent of temperature. By assuming this to be the summed contribution from all implanted holmium ions, a heat capacity per ion of

$$C^{\text{add}}_{\text{ion}} = 1.6 \times 10^{-3} k_{\text{B}} \tag{6.14}$$

can be calculated.

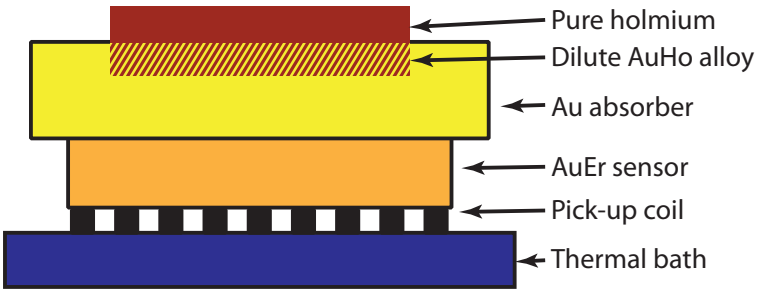

Figure 6.8: Schematic of the MMC with high concentrations of implanted holmium in the gold absorber. A region of pure holmium is located on top of a dilute AuHo alloy.

As discussed in chapter 5.3, depending on the implantation dose, the implanted ions can not be considered to form a dilute Au:Ho alloy in the gold absorber. For the highest doses discussed here, the implantation area can be described by several tens of nano-meters of pure holmium on top of a region where gold and holmium are mixed with a holmium concentration that decreases with increasing depth in the gold absorber. To simplify the following discussion these two regions will be referred to as bulk holmium and dilute alloy respectively, as sketched in figure 6.8y. The heat capacity per ion calculated under the assumption of an equal contribution from all ions is about two orders of magnitude smaller than expected for the different models describing both the limit of the dilute alloy (see figure 6.7) and the bulk holmium (see figure 6.9). For these cases an additional temperature dependent heat capacity is expected with values for $T = 80\,\text{mK}$ around

$$C^{\text{dilute}}_{\text{th}} \approx 430\,\text{pJ/K} \tag{6.15}$$

for the limit of the dilute alloy and

$$C^{\text{bulk}}_{\text{th}} \approx 530\,\text{pJ/K} \tag{6.16}$$

for the case of bulk holmium, which is dominated by the nuclear magnetic moments of the ions. A possible explanation for the discrepancy to these expected values can be derived for the given multi layer model.

Using the theory derived for the dilute alloy under the assumption of $A = 812\,\mathrm{Mhz}$, an effective number of holmium ions in the dilute alloy region can be estimated from the measured heat capacity to be

$$N_{\mathrm{Ho}}^{\mathrm{dilute}} \approx 3 \times 10^{11} \quad . \tag{6.17}$$

This accounts for only 0.3 % of total holmium ions.

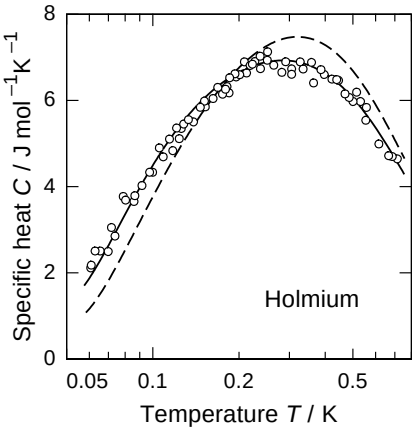

Figure 6.9: Molar heat capacity for bulk ^{165}Ho as function of temperature, after [Van64].

At $T < 19\,\mathrm{K}$ bulk holmium shows ferromagnetic ordering, which represents an extremely stable ground state for the electronic spins at $T < 100\,\mathrm{mK}$. In this stable ground state, excitations of the magnetic moments of the $4f$-electrons, i.e. magnons, would cause a negligible contribution to the specific heat.On the other hand, the contribution caused by the hyperfine splitting of the holmium nuclei is very large, as shown in figure 6.9, and should dominate the total heat capacity of the detector by two orders of magnitude. The fact that this heat capacity is not observed in the pulse shape we can only explain by assuming that the relaxation time of the nuclei is much longer than the time scale of the pulses, such that only a small fraction of heat is flowing there during a pulse.

On the one hand, such long relaxation times for nuclei at $T \approx 100\,\mathrm{mK}$ sound plausible and are well known for non-magnetic high purity noble metals. On the other hand, our group's experience with the isotope ^{167}Er, which has a similarly large hyperfine splitting, being diluted in gold in the paramagnetic temperature sensor, is such, that excitations of the nuclear spin in this system occur on the same time scale as the excitations of the electronic magnetic moments. In addition, relaxing gold nuclei, which also have a significant hyperfine splitting, in the vicinity of the erbium ions can be observed in these experiments. This might not be in conflict with the assumptions made here for the ferromagnetically ordered holmium. One detail that we observed

for the relaxation time of the gold nuclei in the vicinity of the erbium ions is a dependence on the magnetic field, leading to longer relaxation times for an increased magnetic field, being about 1 ms in a 10 mT field. Extrapolating this, it might be realistic that the relaxation time of the holmium nuclei in ferromagnetically ordered holmium is in the order of seconds.

For the case of a negligible contribution from the spin system, the heat capacity of the system of the conduction electrons $C_{\mathrm{e}}^{\mathrm{bulk}}$ would be the dominant contribution in bulk holmium. Using equation 3.6 with $\gamma_{\mathrm{Ho}} = 10\,\mathrm{mJ/mol}$ [Van64] gives a heat capacity below $T = 100\,\mathrm{mK}$ of

$$C_{\mathrm{e}}^{\mathrm{bulk}}(T < 100\,\mathrm{mK}) < 0.15\,\mathrm{pJ/K} \tag{6.18}$$

which is within the uncertainty of the experimental results.

To test this theory, measurements with longer time windows, being in in the order of 10 ms and longer, are necessary to fully understand the pulse shape and identify a possible additional long decay time with possibly very small amplitude. Similar experiments on the remaining chips with lower holmium concentration can also provide information to further understand the thermodynamic properties, as the relative size of the bulk holmium layer will be significantly reduced.

The results demonstrate, that the planned neutrino mass experiment ECHo will benefit greatly from further detailed studies of the heat capacity and relaxations times of holmium and alloys of holmium at milli-Kelvin temperatures, in order to find a well balanced compromise between activity per detector pixel, heat capacity, energy resolution and complexity of signal shape. Understanding the relaxation time-scale of the nuclei in the ferromagnetically ordered holmium is not only highly important to remove any possible systematic effects in the spectral measurement, but could also make use of pure holmium in the absorber a viable consideration for the final detector design, if no significant parasitic effects are found.

7. Summary and outlook

In the present work, theoretical and experimental investigations of the thermodynamic properties of holmium in gold were carried out, to determine the effect of implanted holmium ions on the performance of metallic magnetic calorimeters (MMCs). This work was carried out within the ECHo experiment, which aims to measure the electron neutrino mass by a high statistics and high precision calorimetric measurement of the electron-capture spectrum of ^{163}Ho implanted in MMCs.

The theory for the thermodynamic properties of the implanted holmium ions was developed by describing the system as non-interacting magnetic moments and including the effects of the crystal field, the hyperfine interaction and external magnetic fields. The eigenvalue problem of the system's Hamiltonian was then solved numerically and used to calculate the heat capacity and magnetisation per ion for given sets of crystal field parameters W and x, and hyperfine coupling strength A. Experiments on an AuHo alloy with 1 % Ho-concentration, measuring the magnetisation at temperatures between 2 K and 300 K, were used to determine the crystal field parameters of Au:Ho to $W = -0.112$ and $x = -0.357$. The numerical calculations for these crystal field parameters showed a Schottky anomaly in the heat capacity in a temperature range below 200 mK, with the peak position depending on the value of the hyperfine coupling strength A. A measurement of the specific heat per ion in this temperature range can therefore be used to probe the value of the hyperfine coupling strength. This can be obtained by analysing the height of thermal pulses for a known energy input for detectors containing a well defined number of holmium ions. Using the well established model for the signal shape of MMCs, it is possible to deduce the effect due to the implanted holmium ions by comparing the experimental pulse height with the expected value in the case of no holmium implantation.

The implantation of natural holmium in the gold absorbers of MMCs was performed at RISIKO in the Mainz University. Natural ^{165}Ho has the same nuclear spin as the radioactive isotope ^{163}Ho and can therefore be used as a substitute material in experiments on its thermodynamic properties. The detectors were implanted with 9×10^{11}, 9×10^{12} and 9×10^{13} ^{165}Ho ions, corresponding to respective activities of ^{163}Ho of 4 Bq, 40 Bq and 400 Bq. Different numbers of holmium ions were implanted in three different detectors in order to perform calorimetric measurements of the detector's heat capacity as a function of ion concentration. Simulations for the implantation depth showed that for activities > 10 Bq the implanted holmium ions do not form a simple dilute Au:Ho alloy, but must instead be characterised by a region of pure holmium on top of multiple layers of Au:Ho with decreasing holmium

concentration with increasing depth in the absorber.

A complete characterisation was carried out for one detector with 9×10^{13} implanted ^{165}Ho ions, corresponding to a ^{163}Ho activity of $A = 400\,\mathrm{Bq}$. The analysis of pulse height measurements, performed out in the temperature range between 60 mK and 100 mK, showed no evidence for any significant additional heat capacity. However, the analysis of the pulse shape showed an initial fast time constant in the order of $10\,\mu$s for $T \approx 70$mK, which has never been observed with regular MMC consisting of a Au:Er sensor, stems and gold absorber. This could be interpreted as a heat flow to a system formed by holmium ions diluted in gold. From the analysis of the pulse shape, a corresponding additional heat capacity of $C_{\mathrm{add}} = 2\,\mathrm{pJ/K}$ was observed. Considering this to be related to a system of non-interacting holmium spins and under the assumption of $A = 812\,\mathrm{MHz}$ for the hyperfine coupling strength, we find the corresponding number of holmium ions in this system to be 3×10^{11}. This represents only 0.3 % of the implanted holmium ions. The remaining part of the ions then forms layers with increased holmium concentrations up to 100 %. The ions in this almost pure holmium region order ferromagnetically at $T < 19\,\mathrm{K}$. The nuclear moments of the holmium ions could in principal show a very long relaxation time, due to the stable ground state of the ferromagnetically ordered electronic spins, which would prevent heat loss to this system on the time scale of the measured pulse.

With the measurements performed in this thesis, it was not possible to investigate the effect on the pulse shape which could arise from the heat flowing to the pure holmium system. For that investigation, on the hand pulses need to be acquired over a larger time window to probe longer thermalisation tails, and on the other hand it will be important to measure at detector temperatures of about 20 mK or lower. In the case of a negligible impact on the pulse shape, the method of intentionally depositing the ^{163}Ho source in pure layers could be investigated as a viable method for the ECHo experiment.

In this thesis, a numerical solution for the thermodynamic properties of dilute Au:Ho alloys under the assumption of non-interacting spins was developed. This theory can be extended by including the interactions between spins. The experimental approach to investigate the heat capacity of a Au:Ho system was defined and it is based on the analysis of thermal pulses due to the interaction of x-rays with known energy in low temperature MMCs with implanted holmium ions in different concentrations. Based on the theoretical calculations and experimental approaches developed in this thesis, it will be possible to investigate the properties of Au:Ho systems with high precision. This will be used at first to determine the maximum activity per pixel for the ECHo experiment. The precise understanding of the physics of holmium ions in gold will in future be the basis of investigations of higher order effects in the de-excitation of the daughter atom of the electron capture in ^{163}Ho .

A. Physical properties of the sensor material Au:Er

This summarization of the physical properties of the sensor material Au:Er is primarily based upon and partly reproduced from the explanations in [Sch00, Fle03, Fle05] and is added for the convenience of the reader. Other sources are cited throughout the text.

A.1 Properties of Erbium in Gold

Erbium in low concentrations forms a solid solution with gold [Rid65]. Erbium in the 3+ state substitutes for Au at regular fcc lattice sites giving three of its electrons to the conduction band. The Er^{3+} ion has the electron configuration $[Kr]4d^{10}4f^{11}5s^25p^6$. The paramagnetic behavior results from the partially filled $4f$ shell, having a radius of only about 0.3 Å and located deep inside the outer $5s$ and $5p$ shells. For comparison, the ionic radius of Er^{3+} is about 1 Å, as is depicted in figure A.1. Because of this the influence of the crystal field is greatly reduced and the magnetic moment can be calculated from the orbital angular momentum $\boldsymbol{L}$ the spin angular momentum $\boldsymbol{S}$ and the total angular momentum $\boldsymbol{J}$, which are derived according to Hund's rules. To a good approximation the admixture of exited electronic states can be neglected and the magnetic moment $\boldsymbol{\mu}$ can be written as

$$\boldsymbol{\mu} = g_J \boldsymbol{J} \tag{A.1}$$

with the Landé factor

$$g_J = 1 + \frac{J(J+1) + S(S+1) - L(L+1)}{2J(J+1)} \quad . \tag{A.2}$$

For Er^{3+}, $L = 6$, $S = {}^3/_2$, $J = {}^{15}/_2$ and $g_J = {}^6/_5$. In dilute Au:Er samples the magnetization can indeed be characterized by (A.1) at temperatures above about 100 K [Wil69]. At lower temperatures it is necessary to include crystal field effects in the description. The crystal field with fcc symmetry lifts the sixteen-fold degeneracy of the Er^{3+} ground state, splitting it into a series of multiplets (one Γ_6 and one Γ_7 doublet and three Γ_8 quartets). The lowest lying multiplet is a Γ_7 Kramers doublet. At sufficiently low temperatures and low magnetic fields the behavior of erbium in gold can be approximated as a two level system with effective spin $\tilde{S} = {}^1/_2$ with an isotropic g factor of $\tilde{g} = {}^{34}/_5$. This theoretical value has been confirmed by several ESR experiments (see, for example [Tao71]). The magnitude of energy splitting

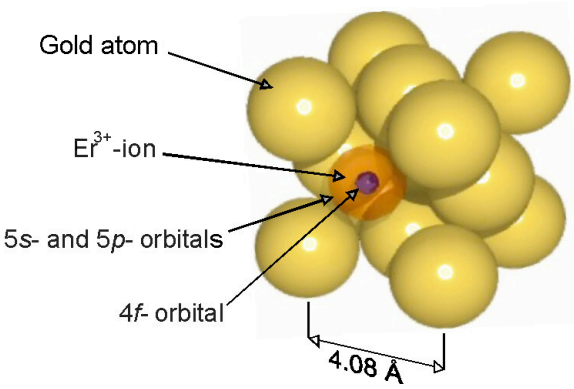

Figure A.1: Schematic of a lattice section of the Au:Er-alloy. The Er^{3+}-ions take regular sites within the Au-lattice. The only partially filled Er $4f$-shell lies deep within the ion.

between the ground state doublet and the first excited multiplet (Γ_8 quartet) has been reported in different experiments [Sjø75, Dav73, Wil69, Hah92] to be between 11 K and 19 K.

Figure A.2 shows the magnetic susceptibility of Au doped with 600 ppm Er in the temperature range between 100 µK and 300 K. The data have been obtained in three different experiments [Her00, Fle03]. While the data at high temperatures ($T > 100\,\mathrm{K}$) are in good agreement with the Curie law for $J = {}^{15}/_{2}$ and $g_J = {}^{6}/_{5}$ there is an increasing deviation from the high temperature approximation below 100 K. This is a result of the depopulation of the multiplets with higher energies. At temperatures below about 1.5 K the data follow a Curie law once again, but with a reduced Curie constant in agreement with the effective spin $\tilde{S} = {}^{1}/_{2}$ and g factor $\tilde{g} = 6.8$ for the ground state doublet. At temperatures below 50 mK and in low magnetic fields such that saturation is unimportant ($\tilde{g}\mu_\mathrm{B}B < k_\mathrm{B}T$), the susceptibility becomes much less temperature dependent. This is a result of the influence of the exchange interaction between the magnetic moments. Finally, at a temperature of about 0.9 mK a maximum in the magnetic susceptibility of the 600 ppm sample is observed, which is the result of a transition to a spin glass state.

A.2 Thermodynamic characterization of non-interacting magnetic moments

The magnetization of the Au:Er alloy, due to the properties of the Er^{3+}-ions, can be used as a temperature information. And since the magnetization is a thermodynamic equilibrium property it can be accurately described theoretically. Starting from a suitable thermodynamic potential, like the free energy with its's full differential

$$\mathrm{d}F = -S\,\mathrm{d}T - VM\mathrm{d}B - \underbrace{p\,\mathrm{d}V}_{=0}\ , \tag{A.3}$$

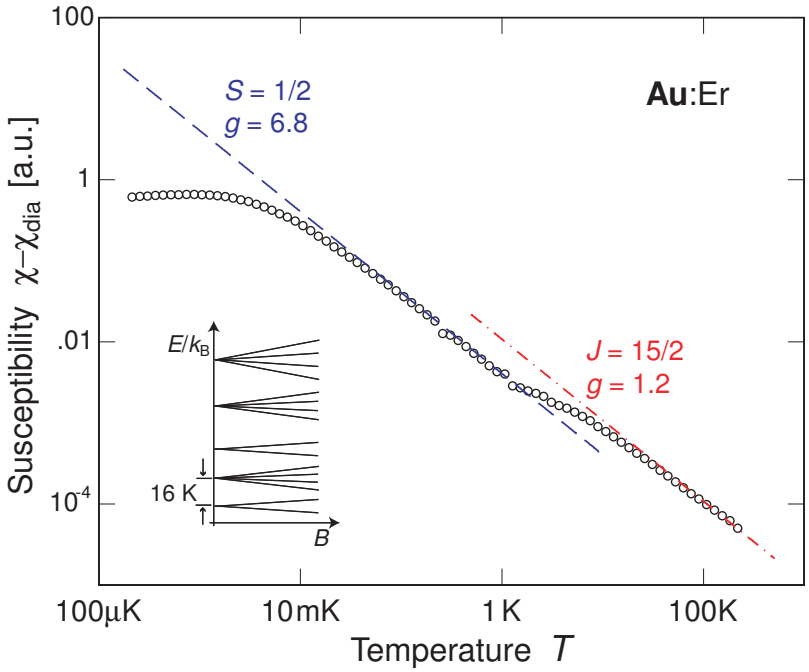

Figure A.2: Paramagnetic contribution to the magnetic susceptibility of Au containing 600 ppm Er as a function of temperature. The *two straight lines* represent the Curie susceptibility assuming Er^{+3} ions in the Γ_7-groundstate doublet and Er^{+3} ions without crystal field splitting. After [Fle03]

with the volume change dV being negligibly small. The free energy F in statistical physics can be found to be

$$F = -Nk_{\mathrm{B}}T \ln z \ , \tag{A.4}$$

being a function of the number of magnetic moments N, the Boltzmann constant $k_{\mathrm{B}} = 1.381 \cdot 10^{-23}\,{}^{\mathrm{J}}/_{\mathrm{K}}$ and the canonical partition function:

$$z = \sum_i \mathrm{e}^{-\frac{E_i}{k_{\mathrm{B}}T}} \ , \tag{A.5}$$

with E_i being the energy eigenstates available to one magnetic moment. This preparatory work (eq. A.3-A.5) can now be used to calculate the properties necessary to estimate the performance as a thermometer from our system, namely the heat capacity C, the magnetization M and it's change with temperature ${}^{\partial M}/_{\partial T}$:

$$C = \frac{N}{k_\mathrm{B}T^2}\left\{\left\langle E^2\right\rangle - \left\langle E\right\rangle^2\right\} \ , \tag{A.6}$$

$$M = -\frac{N}{V}\left\langle\frac{\partial E}{\partial B}\right\rangle \ , \tag{A.7}$$

$$\frac{\partial M}{\partial T} = \frac{N}{Vk_\mathrm{B}T^2}\left\{\left\langle E\frac{\partial E}{\partial B}\right\rangle - \left\langle E\right\rangle\left\langle\frac{\partial E}{\partial B}\right\rangle\right\} \ . \tag{A.8}$$

This general theory on magnetic moments will now be applied to the case of $^{3+}$Er ions in gold. In the previous section A.1 it was shown that at low temperatures only two alignments are possible for the magnetic moments of the ions in an external magnetic field B. The matching energy eigenvalues are

$$E_{m_{\tilde{\mathrm{S}}}} = m_{\tilde{\mathrm{S}}}\tilde{g}\mu_\mathrm{B}B \ , \tag{A.9}$$

with $m_{\tilde{\mathrm{S}}} = \pm{}^1\!/_2$ being the z-component of the quasi spin, $\tilde{g} = 6.8$ the effective isotropic Landé factor of the Γ_7 Kramers doublet, $\mu_\mathrm{B} = 9.274 \cdot 10^{-24}\,\mathrm{Am}^2$ the Bohr magneton and B the absolute value of the magnetic field. Now the properties from eq. A.6–A.8 can be calculated, leading to the well established Schottky anomaly

$$C_\mathrm{Z} = Nk_\mathrm{B}\left(\frac{E}{k_\mathrm{B}T}\right)^2\frac{\mathrm{e}^{E/k_\mathrm{B}T}}{(\mathrm{e}^{E/k_\mathrm{B}T}+1)^2} \tag{A.10}$$

for the heat capacity that is depicted in fig. A.3 and shows a characteristic maximum if the thermal energy $k_\mathrm{B}T$ is about half the energy splitting $\Delta E = g_{\tilde{S}}\mu_\mathrm{B}B$.

Calculating the magnetization of the Au:Er alloy in a similar fashion results in

$$M = \frac{N}{V}\tilde{S}\tilde{g}\mu_\mathrm{B}\mathcal{B}_{\tilde{S}}(h) \tag{A.11}$$

with the Billouin function

$$\mathcal{B}_{\tilde{S}} = \frac{2\tilde{S}+1}{2\tilde{S}}\coth\left[\frac{(2\tilde{S}+1)h}{2\tilde{S}}\right] - \frac{1}{2\tilde{S}}\coth\left[\frac{h}{2\tilde{S}}\right] \tag{A.12}$$

and it's argument

$$h = \frac{\tilde{S}\tilde{g}\mu_\mathrm{B}B}{k_\mathrm{B}T} \ . \tag{A.13}$$

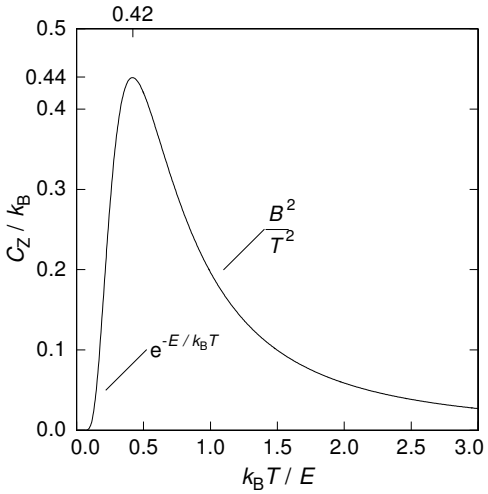

Figure A.3: Heat capacity C of a two-level system with an energy splitting of $\Delta E = \tilde{g}\mu_B B$ as a function of the reduced temperature ${}^{k_B T}/_{\Delta E}$. The approximations for $T \ll {}^{E}/_{k_B}$ and $T \gg {}^{E}/_{k_B}$ are also shown.

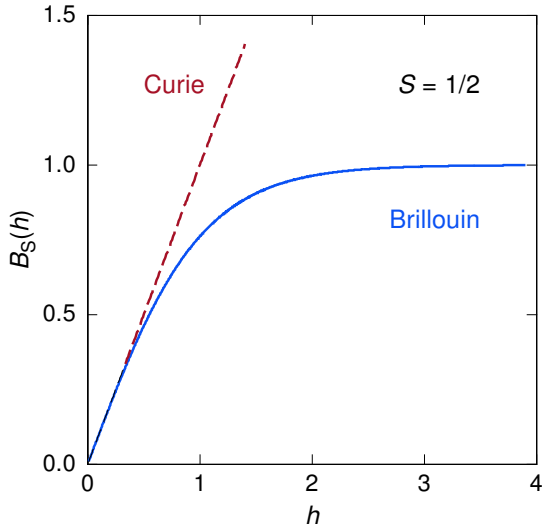

Figure A.4: Brillouin function $\mathcal{B}_{1/2}(h)$ with the Curie approximation for $h \ll 1$. It shows the qualitative progression of the magnetization in a $\tilde{S} = {}^{1}/_{2}$ system in the approximation of non-interacting magnetic moments.

Fig. A.4 depicts the Billouin function in the appropriate case of $\tilde{S} = {}^{1}/_{2}$ that shows the qualitative shape of the magnetization. The maximum value is defined by the density of magnetic ions ${}^{N}/_{V}$ and the maximum z component of the magnetic moment $\tilde{S}\tilde{g}\mu_B$. The field and temperature dependence enters through the argument of the Brillouin function in the ratio ${}^{B}/_{T}$. At low temperatures respectively high fields ($h \gg 1$) the magnetization saturates because all magnetic moments are aligned with the external field, while in the opposite case ($h \ll 1$) the magnetization enters a quasi linear regime known as Curie's law.

A.3 Thermodynamic characterization of interacting magnetic moments

While the assumption of non-interacting spins is sufficient for a qualitative description of the magnetic behavior of Au:Er, it is inadequate for a quantitative analysis. To calculate the magnetic response of Au:Er both the magnetic dipole-dipole interaction and the indirect exchange interacting between the spins must be taken into account.

A.3.1 Dipole-dipole interaction

The interaction of two paramagnetic ions at the positions $\boldsymbol{r}_i$ and $\boldsymbol{r}_j$ through their respective magnetic moment $\boldsymbol{\mu}_{i/j}$ enters the system's Hamiltonian through the following additional term:

$$H_{ij}^{\text{dipole}} = \frac{\mu_0}{4\pi}\frac{1}{r_{ij}^3}\left\{\boldsymbol{\mu}_i \cdot \boldsymbol{\mu}_j - 3(\boldsymbol{\mu}_i \cdot \hat{\boldsymbol{r}}_{ij})(\boldsymbol{\mu}_j \cdot \hat{\boldsymbol{r}}_{ij})\right\} \quad . \tag{A.14}$$

The quantity $\hat{\boldsymbol{r}}_{ij}$ represents the unit vector in the direction $\boldsymbol{r}_i - \boldsymbol{r}_j$ and r_{ij} the distance between the magnetic moments.

Because of the isotropy of the Γ_7 ground state doublet, the dipole-dipole interaction can be expressed in terms of the effective spins $\widetilde{\boldsymbol{S}}_i$ and $\widetilde{\boldsymbol{S}}_j$

$$H_{ij}^{\text{dipole}} = \Gamma_{\text{dipole}}\frac{1}{(2k_{\text{F}}r_{ij})^3}\left\{\widetilde{\boldsymbol{S}}_i \cdot \widetilde{\boldsymbol{S}}_j - 3\left(\widetilde{\boldsymbol{S}}_i \cdot \hat{\boldsymbol{r}}_{ij}\right)\left(\widetilde{\boldsymbol{S}}_j \cdot \hat{\boldsymbol{r}}_{ij}\right)\right\} \tag{A.15}$$

with prefactor $\Gamma_{\text{dipole}} = (\mu_0/4\pi)\,(\tilde{g}\mu_{\text{B}})^2\,(2k_{\text{F}})^3$ and $k_{\text{F}} = 1.2 \cdot 10^{10}\,\text{m}^{-1}$ being the Fermi wave vector of the gold conduction electrons.[1]

A.3.2 RKKY interaction

The exchange interaction of the localized $4f$ electrons of the erbium ions with the gold conduction electrons gives rise to an additional interaction between the erbium ions, the indirect exchange or Ruderman-Kittel-Kasuya-Yosida (RKKY) interaction. Expressed in terms of the effective spin, the RKKY interaction between two erbium

[1] The Fermi wave vector has been introduced artificially here to simplify the quantitative comparison with the indirect exchange interaction discussed later.

spins can be written as

$$H_{ij}^{\mathrm{RKKY}} = \Gamma_{\mathrm{RKKY}} \, (\widetilde{\boldsymbol{S}}_i \cdot \widetilde{\boldsymbol{S}}_j) \, F(2k_{\mathrm{F}} r_{ij}) \tag{A.16}$$

with the function $F(2k_{\mathrm{F}} r_{ij})$ being

$$F(2k_{\mathrm{F}} r_{ij}) = \frac{1}{(2k_{\mathrm{F}} r_{ij})^3} \left[\cos(2k_{\mathrm{F}} r_{ij}) - \frac{1}{2k_{\mathrm{F}} r_{ij}} \sin(2k_{\mathrm{F}} r_{ij}) \right] \tag{A.17}$$

and prefactor Γ_{RKKY} given by

$$\Gamma_{\mathrm{RKKY}} = \mathcal{J}^2 \, \frac{4 V_0^2 m_{\mathrm{e}}^* k_{\mathrm{F}}^4}{\hbar^2 (2\pi)^3} \, \frac{\widetilde{g}^2 (g_J - 1)^2}{g_J^2} \ . \tag{A.18}$$

Here $\mathcal{J}$ denotes the coupling energy between the localized spins and the conduction electrons, V_0 is the volume of the elementary cell and m_{e}^* is the effective mass of the conduction electrons. The expression for the RKKY interaction given above is derived under the assumption that the mean free path of the electrons is larger than the mean distance between the localized erbium ions. In principle, it is possible that the RKKY interaction is reduced due to a finite coherence length λ of the spin polarization of the conduction electrons. In this case an additional factor $\mathrm{e}^{-r/\lambda}$ would appear in (A.16). However, for Au:Er with suitable erbium concentrations for its main application in low temperature metallic magnetic calorimeters (MMCs), the mean free path of the conduction electrons is always much larger than the mean separation of the erbium ions.[2]

The fact that both the dipole-dipole interaction and the RKKY interaction are proportional to $1/r_{ij}^3$ allows us to compare their relative strength by a dimensionless parameter which is defined as the ratio of the two pre-factors

$$\alpha = \frac{\Gamma_{\mathrm{RKKY}}}{\Gamma_{\mathrm{dipole}}} \ . \tag{A.19}$$

Using this parameter α the coupling energy $\mathcal{J}$ can be expressed as[3]

$$\mathcal{J} \simeq \sqrt{\alpha} \, 0.145 \text{ eV} \ . \tag{A.20}$$

[2] In measurements of the residual resistivity of dilute $\mathrm{Au}_{1-x}\mathrm{Er}_x$ alloys $\varrho = x \, 6.7 \times 10^{-6} \, \Omega \, \mathrm{m}$ was found [Ara66, Edw68], and one can conclude that the mean free path of the conduction electrons is about 4000 Å for an erbium concentration of $x = 300$ ppm.

[3] The value of $\mathcal{J}$ given by (A.20) refers to the definition of the exchange energy between a localized spin $\boldsymbol{S}$ and a free electron $\boldsymbol{s}$ being $H = \mathcal{J} \boldsymbol{s} \cdot \boldsymbol{S}$. The definition $H = 2\mathcal{J} \boldsymbol{s} \cdot \boldsymbol{S}$ is often found in literature, leading to values of the parameter $\mathcal{J}$ being smaller by a factor of two.

A.4 Numerical calculation of the thermodynamical properties

A determination of the heat capacity and magnetization of a system of randomly distributed, interacting erbium spins requires a numerical calculation. There is a number of ways to perform this kind of calculation in the framework of a mean-field approximation. The method that requires the least amount of CPU time assumes the specific form of the mean field distribution that has been derived by Walker and Walstedt [Wal77, Wal80] for magnetic moments randomly distributed in a continuous medium. These authors showed that this analytic representation of the mean field distribution agrees well with numerically calculated mean field distributions.

An alternative approach is to write down the Hamiltonian for a cluster of interacting, randomly distributed spins on the Au lattice and obtain the eigenvalues of the cluster. This process is repeated for a large number of configurations of randomly positioned spins with the heat capacity and magnetization obtained by averaging. Since this process delivers the more accurate results and is currently used to determine the Au:Er behavior theoretically it will be explained in more detail in the following.

The basis for this approach is a cubic lattice segment of the gold fcc-lattice, typically with an edge length of ten to twenty lattice constants, depending on the simulated spin concentration. Additionally quasi-periodic boundary conditions are assumed, repeating the cube four times in every direction in space. On this lattice segment $n = \text{const.}$ spins are randomly distributed. For each configuration the Hamiltonian matrix is constructed. It includes the interaction of the magnetic moments with the external magnetic field (Zeeman interaction) and the dipole-dipole and RKKY interaction in between spin pairs.

In the basis $\mid S_1, S_2, \ldots, S_{n_{\max}}\rangle$ with the spin eigenvalues $S_i \in \{|\uparrow\rangle, |\downarrow\rangle\}$ and $\boldsymbol{B} = (0, 0, B_z)$ the Hamiltonian of two spins $\boldsymbol{S}_1$ und $\boldsymbol{S}_2$ at positions $\boldsymbol{r}_1$ und $\boldsymbol{r}_2$ takes the following form:

$$\mathcal{H} = \mathcal{H}^{\text{Zeeman}} + \mathcal{H}^{\text{dipole}} + \mathcal{H}^{\text{RKKY}}, \text{ with} \tag{A.21}$$

$$\mathcal{H}^{\text{Zeeman}} = -\tilde{g}\mu_{\text{B}}(S_{z\,1} + S_{z\,2})B_z \ , \tag{A.22}$$

$$\mathcal{H}^{\text{dipole}} = \frac{\mu_0}{4\pi}\frac{(\tilde{g}\mu_{\text{B}})^2}{r^3}\Big(\begin{array}{lll} -(3\,\cos^2\theta - 1) & (\ S_{z\,1}S_{z\,2} & \ ) \\ +1\!/\!_4\,(3\cos^2\theta - 1) & (\ S_{+\,1}S_{-\,2} + S_{-\,1}S_{+\,2} & \ ) \\ -3\!/\!_2\,\sin\theta\cos\theta & (\ S_{z\,1}S_{+\,2} + S_{z\,2}S_{+\,1} & \ ) \\ -3\!/\!_2\,\sin\theta\cos\theta & (\ S_{z\,1}S_{-\,2} + S_{z\,2}S_{-\,1} & \ ) \\ -3\!/\!_4\,\sin^2\theta & (\ S_{+\,1}S_{+\,2} & \ ) \\ -3\!/\!_4\,\sin^2\theta & (\ S_{-\,1}S_{-\,2} & \ ) \end{array}\Big) \ , \tag{A.23}$$

$$\mathcal{H}^{\text{RKKY}} = \alpha\,\frac{\mu_0}{4\pi}(\tilde{g}\mu_{\text{B}})^2\,(2k_F)^3\Big(S_{z\,1}S_{z\,2} + \frac{1}{2}(S_{+\,1}S_{-\,2} + S_{-\,1}S_{+\,2})\Big)\,F(\rho) \tag{A.24}$$

and

$$F(\rho) = \rho^{-3}\left(\cos(\rho) - \frac{\sin(\rho)}{\rho}\right) \ , \ \rho = 2k_{\text{F}}r \ . \tag{A.25}$$

In this context θ is the angle between $\mathbf{B}$ and $\hat{\mathbf{r}} = \frac{\mathbf{r}_2 - \mathbf{r}_1}{|\mathbf{r}_2 - \mathbf{r}_1|}$. S_+ and S_- are the usual raising and lowering operators. The Hamiltonian matrix has the rank 2^n and therefore 2^{2n} elements. For reasons of clarity and comprehension the shown Hamiltonian is limited to two interacting magnetic moments:

$$\mathcal{H} = \begin{array}{c} \begin{array}{cccc} |\uparrow\uparrow\rangle & |\uparrow\downarrow\rangle & |\downarrow\uparrow\rangle & |\downarrow\downarrow\rangle \end{array} \\ \begin{pmatrix} -D_2 + \frac{1}{4}R + 2Z & -D_1 & -D_1 & -D_3 \\ -D_1 & +D_2 - \frac{1}{4}R & +D_2 + \frac{1}{2}R & +D_1 \\ -D_1 & +D_2 + \frac{1}{2}R & +D_2 - \frac{1}{4}R & +D_1 \\ -D_3 & +D_1 & +D_1 & -D_2 + \frac{1}{4}R - 2Z \end{pmatrix} \end{array}, \tag{A.26}$$

with the variables $\underbrace{Z = -\frac{1}{2}\tilde{g}\mu_{\text{B}}B_{\text{z}}}_{\text{Zeeman}}$, $\underbrace{R = \alpha\,\frac{\mu_0}{4\pi}(\tilde{g}\mu_{\text{B}})^2(2k_{\text{F}})^3\,\text{F}(\rho)}_{\text{RKKY}}$ and

$$\underbrace{D_1 = \frac{3}{4}\frac{\mu_0}{4\pi}\frac{\tilde{g}\mu_{\text{B}}}{r^3}\cos\theta\sin\theta \ , \ D_2 = \frac{1}{4}\frac{\mu_0}{4\pi}\frac{\tilde{g}\mu_{\text{B}}}{r^3}(3\cos^2\theta - 1) \ , \ D_3 = \frac{3}{4}\frac{\mu_0}{4\pi}\frac{\tilde{g}\mu_{\text{B}}}{r^3}\sin^2\theta}_{\text{dipole}-\text{dipole}} \ .$$

The parameters of the Monte-Carlo style simulation are chosen in the following way: $n = 6$ was chosen based on the minor improvement in accuracy for $n > 6$ and the available computation time. The lattice size was adjusted between 10 and 40 lattice

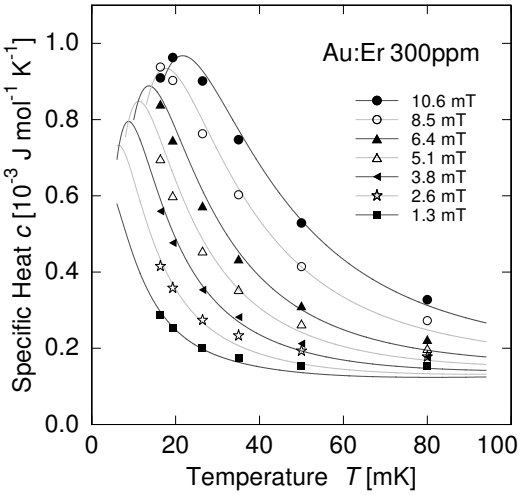

Figure A.5: Specific heat of Au:Er with 300 ppm enriched ^{166}Er as a function of temperature at different applied magnetic fields. The *solid lines* are calculated numerically with a interaction parameter $\alpha = 5$ [Ens00]

constants to cover the usually used concentrations below 5000 ppm. These n spins are then randomly distributed across the lattice. Since the sensor material is normally available in a polycrystalline form also the orientation of the magnetic field is not previously defined and is chosen randomly and the angle θ is calculated accordingly for each pair of spins.

Based on this randomly chosen configuration the Hamiltonian matrix is constructed for different values of the external magnetic field and the energy eigenvalues are calculated by numerically diagonalizing the matrix. With the energy eigenvalues the thermodynamic properties C, M, and $^{\partial M}/_{\partial T}$ can be calculated at any given temperature according to eq. A.6–A.8.

These calculation is repeated a large number of times and the results then averaged to get the final predictions for the thermodynamic properties. For the extreme cases, namely temperatures below 20 mK and concentrations above 1000 ppm the number of repetitions needs to be at least 10^4 to get stable results.

As an example we show in Fig. A.5 the specific heat of an Au:Er sample having a concentration of 300 ppm of 97.8% enriched ^{166}Er. The temperature of the maximum in the specific heat depends on the magnitude of the external magnetic field as expected for a Schottky anomaly. However, the maximum is about twice as wide as for a non-interacting spin system. Calculations based on averaging over spin clusters provide a quantitative agreement assuming an interaction parameter α of 5. Although the calculated curves depend rather strongly on the choice of α, the value of $\alpha = 5$ should be viewed as an upper bound for the following two reasons. Firstly, the presence of ^{167}Er in the enriched sample leads to a slight additional broadening of the curve because of the hyperfine contribution of this isotope. Secondly, additional broadening results from a variation of the applied magnetic field, of about 10 to 15%,

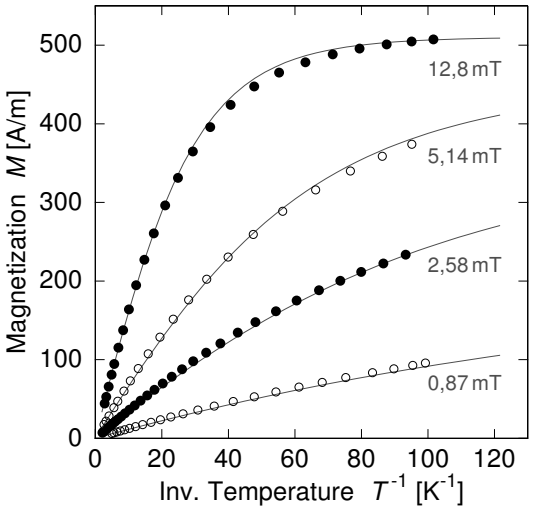

Figure A.6: Magnetization of Au:Er with 300 ppm enriched ^{166}Er as a function of $^1/_T$ at different applied magnetic fields. The *solid lines* are calculated numerically with a interaction parameter $\alpha = 5$ [Ens00]

over the sample due to the geometry of the field coil.

The magnetization is plotted as a function of $^1/_T$ in Fig. A.6 at several different magnetic fields for the 300 ppm sample. As in the case of the specific heat, the magnetization deviates for the behavior of isolated spins. The deviation is primarily due to the interaction between the magnetic moments, but a small contribution is also present due to the two reasons discussed above for the heat capacity. Again the data can be described satisfactorily by assuming an interaction parameter of $\alpha = 5$.

The magnetic properties of a weakly interacting spin system is perhaps most easily characterized in terms of the temperature dependence of the susceptibility given by the Curie-Weiss law, $\chi = {}^{\lambda}/_{(T+\theta)}$. The Curie constant λ is proportional to the concentration of the spins, as is the Weiss constant θ, which is a measure of strength of the interactions. For the Au:Er system, $\lambda = x\,5.3\,\mathrm{K}$ and $\theta = \alpha\,x\,1.1\,\mathrm{K}$, where x is the concentration of erbium ions.

A.5 Response Time

Au:Er can be used as temperature sensor in several ways, one of which is the use in low temperature detectors as proposed by Bandler et al. [Ban93]. For this application not only the resolving power in temperature is important, but also the response time since it directly influences the count rate of the detector.

The rise time is influenced by two factors. Firstly the heat needs to get to the temperature sensor and secondly the heat needs to influence the spins and create the magnetic signal.

In a usual setup for soft X-ray detection the temperature sensor is connected to

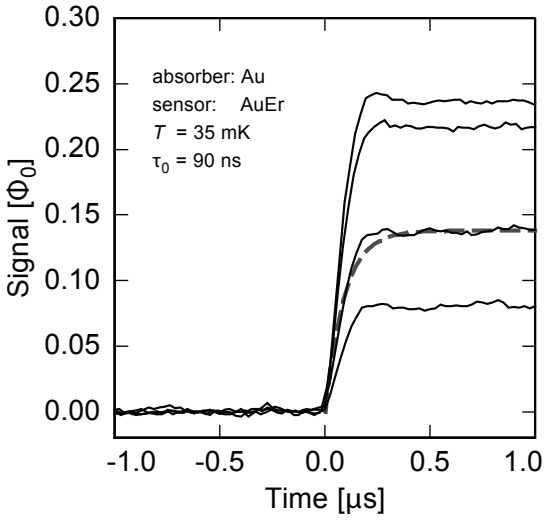

Figure A.7: Detector signals in units of magnetic flux in the SQUID during the first micro-second after the absorption of X-rays of different energy in an MMC designed for soft X-ray spectroscopy [Fle09]. The observed rise time of $\tau = 90\,\mathrm{ns}$ is in agreement predictions from the Korringa relation described in the text.

a particle absorber made of electroplated pure gold with dimensions of $250\,\mu\mathrm{m} \times 250\,\mu\mathrm{m} \times 5\,\mu\mathrm{m}$ with a residual resistivity ratio of ${}^{R_{300\,\mathrm{K}}}/_{R_{4\,\mathrm{K}}} \approx 15$. In such an absorber the thermalization process is governed by the thermal diffusion within the absorber since the down conversion to thermal energies is completed on the order of $\sim 0.5\,\mathrm{ns}$ within a volume of a few cubic micrometers [Ens00, Koz12]. The time scale for the diffusion process is mainly determined by the geometry of the absorber and the presence of defects such as grain boundaries and dislocations. If we assume the before mentioned geometry, the thermalization time, using the Wiedemann–Franz law, can be estimated to be on the order of 10 ns.

The time for the heat to flow from the absorber into the sensor is more difficult to estimate since this depends very much on the nature of the thermal connection between the two components. For sputter deposited or electroplated gold absorbers, as used in micro-fabricated detectors, the thermal contact is sufficiently strong that no degradation of the response time of the magnetic calorimeters due to the presence of the interface is observable.

Finally, the energy is shared with the magnetic moments in the sensor material giving rise of the signal. The response time of the spins is determined by the electron-spin relaxation time τ, which is described by the Korringa relation $\tau = {}^{\kappa}/_{T}$, where κ denotes the Korringa constant. For Au:Er the Korringa constant has been determined in ESR measurements at 1 K to be $\kappa = 7 \times 10^{-9}\,\mathrm{Ks}$ [Sjø75]. This value of κ yields a spin-electron relaxation time of the order of 100 ns at the usual operation temperatures below 100 mK.

Therefore the electron-spin relaxation is the dominating factor in the response time of metallic magnetic calorimeters based on the sensor material Au:Er. This has successfully been shown in [Fle09] where rise times as low as $\tau = 90\,\mathrm{ns}$ have been

observed and is shown in fig. A.7 reproduced from the same source.

While this balance between heat diffusion and electron-spin relaxation works out well for small detectors for soft X-ray spectroscopy this balance is off in case of larger detectors for hard X-ray or γ-ray spectroscopy. For detectors like maXs-200, described in [Pie12b, Pie12a], with absorber dimensions of $2000\,\mu m \times 500\,\mu m \times 200\,\mu m$ the heat diffusion within the absorber is the governing factor in the response time. Depending on the interaction site in the absorber the heat can reach the sensor with different time patterns and create different detector responses [Pie12a]. These different pulse shapes will complicate the analysis and degrade the detector resolution. Therefore it is helpful to weaken the link between absorber and Au:Er sensor to allow the absorber to thermalize internally before allowing the heat to flow to the sensor creating consistent pulse shapes independent of the interaction site within the absorber.

Influence of Nuclear Spins

In the design of a magnetic calorimeter the possible influence of nuclear spins has to be considered. In the case of Au:Er there are two ways in which nuclei can affect the performance of the calorimeter. Firstly, the isotope ^{167}Er with nuclear spin $I = {}^7/_2$ influences the magnetization and the heat capacity due to its hyperfine interaction with the $4f$ electrons. Secondly, and more subtle, the 100% abundant ^{198}Au nuclei with small magnetic moment but large quadrupole moment may contribute to the specific heat if the nuclei reside at positions where the electric field gradient is of non-cubic symmetry.

The hyperfine contribution of the erbium isotope ^{167}Er, if used in its natural abundance of 23 %, significantly reduces the magnetization signal and increases the specific heat of the sensor material. But since presently all metallic magnetic calorimeters use Au:Er that is depleted in ^{167}Er, it has no visible effect on the thermodynamic properties of the sensor material. The influence of ^{167}Er has nonetheless been investigated in [Sjø75] and its effect on metallic magnetic calorimeters has been summarized in e.g. [Fle05].

Nuclei of the host metal can also influence the performance of an MMC. The ^{198}Au nuclei have spin $I = {}^3/_2$, a quadrupole moment of 0.547 barn and a magnetic moment sufficiently small to be neglected. In pure gold no contribution of the nuclear spins to the specific heat is expected at low fields, since the electric field of cubic symmetry does not lift the degeneracy of the nuclear levels. However, for Au nuclei in the vicinity of an Er^{3+} ion the electric field gradient can be substantial and can split the nuclear levels. This results in an additional heat capacity. Fig. A.8 shows the measured heat capacity of the Au nuclei as a function of temperatures for samples with

different erbium concentrations. The data below 10 mK for the sample with 600 ppm is the total specific heat since at such low temperatures the contribution of the Au nuclei is substantially larger than that of all other degrees of freedom. The figure also shows a theoretical curve calculated assuming a quadrupole splitting of 70 MHz for Au nuclei in the immediate vicinity of erbium ions, the splitting decreasing for nuclei at larger distances in a manner similar to that measured in other dilute alloys such as Cu:Pt [Kon96], Cu:Pd [Min80], and Gd:Au [Per76].

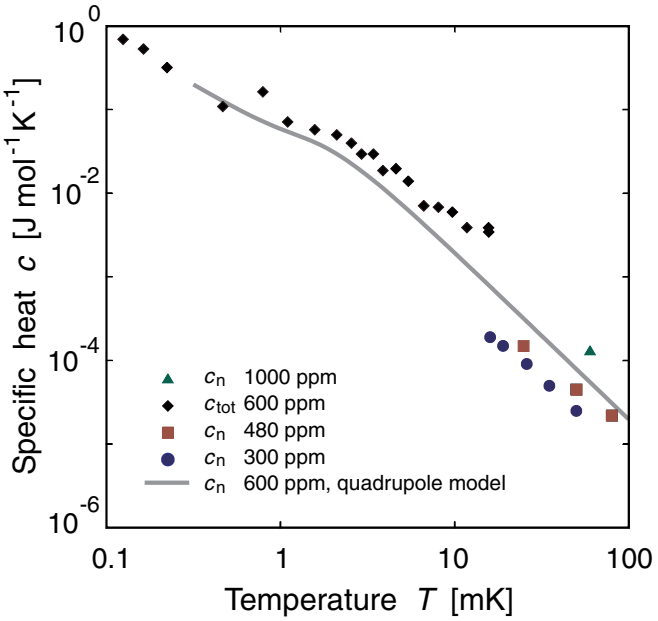

Figure A.8: Contribution of the Au nuclei to the specific heat of Au:Er samples with different concentrations. The *solid line* represents a theoretical curve assuming a quadrupole splitting of 70 MHz for Au nuclei, which are nearest neighbors of Er. Here c_{tot} denotes the total specific heat and c_{n} the contribution of just the Au nuclei to the specific heat. After [Ens00]

This unwanted contribution to the specific heat can only be eliminated by using a host material which has a nuclear spin $I \leq {}^1/_2$. At first glance it would appear desirable to use silver as a host material rather than gold since the two isotopes of silver (^{107}Ag and ^{109}Ag) both have nuclear spin $I = {}^1/_2$. However, the exchange energy $\mathcal{J}$ is 1.6 larger in silver than in gold as determined by ESR measurements[Tao71]. Since the interaction parameter α is quadratic in the exchange energy $\alpha \propto \mathcal{J}^2$, as shown in [Bur08] where $\alpha = 15$ was found, silver is not as attractive as a host material for a magnetic sensor. Just recently the interest in Ag:Er as sensor material has increased regardless, since MMCs have been used at even lower temperatures on the order of $T = 10$ mK where the additional specific heat in Au:Er might outweigh the stronger RKKY-interaction in Ag:Er.

A.5.1 Excess $^1/_f$-noise and AC-susceptibility

While investigating the noise behavior of metallic magnetic calorimeters with Au:Er as sensor material an excess noise contribution has been observed. The contribution was empirically found to be independent of temperature between 4.2 K and 20 mK and its noise power is proportional to the concentration of erbium ions in the sensor. It can be described by attributing a fluctuating magnetic moment with a spectral noise density of $S_m \simeq 0.1\,{}^{\mu_\mathrm{B}^2}/_{f^\eta}$ to each erbium ion, where μ_B is the Bohr magneton, f is the frequency and the exponent η takes values between 0.8 and 1 [Dan05, Fle09]. The same behavior was also found in detectors based on the sensor material Ag:Er [Bur08].

Similar behavior was found in several spin glasses (e.g. [Rei86, Sve89]) and agreed with the fluctuation-dissipation theorem [Joh28, Nyq28] by comparing ac-susceptibility measurements with equilibrium magnetic noise of the same sample. But the amplitude of the $^1/_f$-noise decreased quickly for $T > T_\mathrm{c}$, where T_c is the transition temperature to the spin glass state, until not distinguishable from the background noise.

Au:Er also undergoes a transition to a spin glass but up to two orders of magnitude below the temperatures metallic magnetic calorimeters are usually operated at (see sec. A.1). Therefore the $^1/_f$-noise should not be observable if explained by the same underlying cause. Recent investigations [Hof12, Wiß13] nonetheless found that the $^1/_f$-noise found in metallic magnetic calorimeters is in fact caused by the fluctuation-dissipation theorem, also by comparing the ac-susceptibility with equilibrium magnetic noise in a temperature range between 20 mK and 1 K for two Au:$\mathrm{Er}_{255\,\mathrm{ppm}}$ and Au:$\mathrm{Er}_{845\,\mathrm{ppm}}$ samples.

Bibliography

[Abr70] A. Abragam and B. Bleaney: *Electron Paramagnetic Resonance of Transition-Ions*, Clarendon Press, Oxford (1970)

[Ago13] M. Agostini, M. Allardt, E. Andreotti *et al.*: *Results on neutrinoless double beta decay of 76Ge from GERDA Phase I*, Physical Review Letters **111**(12), 122503 (2013), DOI: 10.1103/PhysRevLett.111.122503, 1307.4720

[Aih11] H. Aihara, C. Allende Prieto, D. An *et al.*: *the Eighth Data Release of the Sloan Digital Sky Survey: First Data From SDSS-III*, The Astrophysical Journal Supplement Series **193**(2), 29 (2011), DOI: 10.1088/0067-0049/193/2/29

[Alp15] B. Alpert, M. Balata, D. Bennett *et al.*: *HOLMES - The Electron Capture Decay of 163Ho to Measure the Electron Neutrino Mass with sub-eV sensitivity*, Eur. Phys. J. C **75**, 112 (2015)

[And82] J. Anderson, G. Beyer and G. Charpak: *A limit on the mass of the electron neutrino: The case of 163Ho*, Physics Letters B **113**(1), 72–76 (1982), DOI: 10.1016/0370-2693(82)90112-5

[Ang05] J. Angrik, T. Armbrust, A. Beglarian *et al.*: *KATRIN Design Report 2004*, Tech. Rep. FZKA 7090; NPI ASCR Rez EXP-01/2005; MS-KP-0501, Forschungszentrum Karlsruhe GmbH (2005)

[Ara66] S. Arajs and G. Dunmyre: *A search for low-temperature anomalies in the electrical resistivity of dilute gold-erbium alloys*, Journal of the Less Common Metals **10**(3), 220 – 224 (1966), DOI: 10.1016/0022-5088(66)90113-5

[Art14] D. R. Artusa, F. T. Avignone, O. Azzolini *et al.*: *Exploring the Neutrinoless Double Beta Decay in the Inverted Neutrino Hierarchy with Bolometric Detectors* 22 (2014), 1404.4469

[Aug12] M. Auger, D. J. Auty, P. S. Barbeau *et al.*: *Search for Neutrinoless Double-Beta Decay in ^{136}Xe with EXO-200*, Physical Review Letters **109**(3) (2012), DOI: 10.1103/PhysRevLett.109.032505, 1205.5608

[Ban93] S. Bandler, C. , R. Lanou *et al.*: *Metallic magnetic bolometers for particle detection*, Journal of Low Temperature Physics **93**(3-4), 709–714 (1993), DOI: 10.1007/BF00693500

[Ber12] J. Beringer, J. F. Arguin, R. M. Barnett *et al.*: *Review of Particle Physics*, Phys. Rev. D **86**, 010001 (2012), DOI: 10.1103/PhysRevD.86.010001

[Ble89] B. Bleaney: *Lanthanide ions in metallic gold II. Terbium and holmium*, Proc. R. Soc. Lond. A **424**, 299–306 (1989)

[Bur08] A. Burck: *Entwicklung großflächiger mikrostrukturierter magnetischer Kalorimeter mit Au:Er- und Ag:Er-Sensoren für den energieaufgelösten Nachweis von Röntgenquanten und hochenergetischen Teilchen*, Ph.D. thesis, Heidelberg University (2008), URN: urn:nbn:de:bsz:16-opus-88322

[Cla04] J. Clarke and A. Braginski: *The SQUID Handbook: Fundamentals and Technology of SQUIDs and SQUID Systems*, Wiley Weinheim (2004)

[Dan05] T. Daniyarov: *Metallische magnetische Kalorimeter zum hochauflösenden Nachweis von Röntgenquanten und hochenergetischen Molekülen*, Ph.D. thesis, Heidelberg University (2005), URN: urn:nbn:de:bsz:16-opus-52319

[Dav73] D. Davidov, C. Rettori, A. Dixon *et al.*: *Crystalline-Field Effects in the Electron-Spin Resonance of Rare Earths in the Noble Metals*, Physical Review B **8**, 3563–3568 (1973), DOI: 10.1103/PhysRevB.8.3563

[De 82] A. De Rújula and M. Lusgnoli: *Calorimetric measurements of* ^{163}*Holmium decay as tools to determine the electron neutrino mass*, Physics Letters B **118**(4-6), 429–434 (1982), DOI: 10.1016/0370-2693(82)90218-0

[Dre13] G. Drexlin, V. Hannen, S. Mertens and C. Weinheimer: *Current Direct Neutrino Mass Experiments*, Advances in High Energy Physics (2013), DOI: 10.1155/2013/293986, 1307.0101

[Due15] C. Duellmann: *Personal Communications* (2015)

[Edw68] L. R. Edwards and S. Legvold: *Electrical Resistivity of Some Dilute Gold-Rare-Earth Alloys*, Journal of Applied Physics **39**(7), 3250–3252 (1968), DOI: 10.1063/1.1656764

[Ens00] C. Enss, A. Fleischmann, K. Horst *et al.*: *Metallic Magnetic Calorimeters for Particle Detection*, Journal of Low Temperature Physics **121**(3-4), 137–176 (2000), DOI: 10.1023/A:1004863823166

[Ens05] C. Enss and S. Hunklinger: *Low-Temperature Physics*, Springer, Berlin, heidelberg, New York (2005)

[Fae14] A. Faessler, L. Gastaldo and M. Simkovic: *Electron Capture in 163Ho and Overlap plus Exchange Corrections and Neutrino Mass*, Nuclear and particle physics **42**(1) (2014)

[Fae15a] A. Faessler: *Improved Description of One- and Two-hole States after Electron Capture in 163 Holmium and the Determination of the Neutrino Mass*, Phys. Rev. C **91**(4) (2015)

[Fae15b] A. Faessler, C. Enss, L. Gastaldo and F. Simkovic: *Determination of the neutrino mass by electron capture in 163Holmium and the role of the three-hole states in 163Dysprosium* (2015), `arXiv:1503.02282`

[Fle98] A. Fleischmann: *Hochauflösendes magnetisches Kalorimeter zur Detektion von einzelnen Röntgenquanten*, Diploma thesis, Heidelberg University (1998)

[Fle03] A. Fleischmann: *Magnetische Mikrokalorimeter: Hochauflösende Röntgenspektroskopie mit energiedispersiven Detektoren*, Dissertation, Heidelberg University (2003)

[Fle05] A. Fleischmann, C. Enss and G. Seidel: *Metallic magnetic calorimeters*, Topics in Applied Physics **99**, 151–206 (2005)

[Fle09] A. Fleischmann, L. Gastaldo, S. Kempf *et al.*: *Metallic magnetic calorimeters*, AIP Conference Proceedings **1185**(1), 571–578 (2009), DOI: `10.1063/1.3292407`

[Fuk98] Y. Fukuda, T. Hayakawa, E. Ichihara *et al.*: *Evidence for Oscillation of Atmospheric Neutrinos*, Physical Review Letters **81**(8), 1562–1567 (1998)

[Gas13] L. Gastaldo, P.-O. Ranitsch, F. von Seggern, J.-P. Porst and S. Schäfer: *Characterization of low temperature metallic magnetic calorimters having gold absorbers with implanted ^{163}Ho ions*, Nucl. Instrum. Meth. A **711**, 150–159 (2013)

[Gas14] L. Gastaldo, K. Blaum, A. Doerr *et al.*: *The Electron Capture ^{163} Ho Experiment ECHo*, Journal of Low Temperature Physics **176**(5-6), 876–884 (2014), DOI: `10.1007/s10909-014-1187-4`

[Gat97] F. Gatti, P. Meunier, C. Salvo and S. Vitale: *Calorimetric measurement of the 163Ho spectrum by means of a cryogenic detector*, Physics Letters B **398**(3-4), 415–419 (1997), DOI: `10.1016/S0370-2693(97)00239-6`

[Giu12] A. Giuliani and A. Poves: *Neutrinoless Double-Beta Decay*, Advances in High Energy Physics 1–38 (2012), DOI: 10.1155/2012/857016

[Hah92] W. Hahn, M. Loewenhaupt and B. Frick: *Crystal field excitations in dilute rare earth noble metal alloys*, Physica B: Condensed Matter **180–181, Part 1**, 176 – 178 (1992), DOI: 10.1016/0921-4526(92)90698-R

[Her00] T. Herrmannsdörfer, R. König and C. Enss: *Properties of Er-doped Au at ultralow temperatures*, Physica B: Condensed Matter **284–288, Part 2**, 1698 – 1699 (2000), DOI: 10.1016/S0921-4526(99)02942-7

[Heu11] S. Heuser: *Entwicklung mikrostrukturierter magnetischer Kalorimeter mit verbesserter magnetischer Flusskopplung für die hochauflösende Röntgenspektroskopie*, Master thesis, Heidelberg University (2011)

[Hof12] V. Hoffmann: *Messung der AC-Suszeptibilität von paramagnetischem Au:Er bei Temperaturen oberhalb des Spinglas-Übergangs*, Bachelor thesis, Heidelberg University (2012)

[Joh28] J. B. Johnson: *Thermal Agitation of Electricity in Conductors*, Physical Review **32**, 97–109 (1928), DOI: 10.1103/PhysRev.32.97

[Jos62] B. Josephson: *Possible new effects in superconductive tunneling*, Physics Letters **1**(7), 251–253 (1962)

[Kem14] S. Kempf, M. Wegner, L. Gastaldo, A. Fleischmann and C. Enss: *Multiplexed Readout of MMC Detector Arrays Using Non-hysteretic rf-SQUIDS*, J. Low Temp. Phys. **176**, 426–432 (2014)

[KK06] H. Klapdor-Kleingrothaus and I. Krivosheina: *The evidence for the observation of 0\nu\beta\beta decay: The identification of 0\nu\beta\beta Events from the Full Spectra*, Mod. Phys. Lett. A **21**, 1547 (2006)

[Kom11] E. Komatsu, K. M. Smith, J. Dunkley *et al.*: *Seven-Year Wilkinson Microwave Anisotropy Probe (WMAP) Observations: Cosmological Interpretation*, The Astrophysical Journal Supplement Series **192**(2), 18 (2011), DOI: 10.1088/0067-0049/192/2/18

[Kon96] K. Konzelmann, G. Majer and A. Seeger: *Solid Effect Between Quadrupolar Transitions in Dilute Cu-Pd Alloys*, Zeitschrift für Naturforschung A **51**(5/6), 506–514 (1996)

[Koz12] A. Kozorezov: *Energy Down-Conversion and Thermalization in Metal Absorbers*, Journal of Low Temperature Physics **167**(3-4), 473–484 (2012), DOI: 10.1007/s10909-011-0426-1

[Kra13] M. Krantz: *Entwicklung, Mikrofabrikation und Charakterisierung von metallischen magnetischen Kalorimetern für die hochauflösende Röntgenspektroskopie hochgeladener Ionen*, Master thesis, Heidelberg University (2013)

[Kug00] E. Kugler: *The ISOLDE facility*, Hyperfine Interactions **129**, 23–42 (2000)

[Kun14] G. J. Kunde, N. Collaboration, E. Birnbaum *et al.*: *Towards Measuring the Neutrino Mass via Holmium Electron Capture Spectroscopy* (2014), URL http://p25ext.lanl.gov/~kunde/NuMECS/

[Lea62] K. Lea, M. Leask and W. Wolf: *The raising of angular momentum degeneracy of f-Electron terms by cubic crystal fields*, Journal of Physics and Chemistry of Solids **23**(10), 1381–1405 (1962)

[Lor01] T. J. Loredo and D. Q. Lamb: *Bayesian analysis of neutrinos observed from supernova SN 1987A*, Physical Review D 46 (2001), DOI: 10.1103/PhysRevD.65.063002, 0107260

[McC68] D. McCumber: *Effect of ac impedance on dc voltage-current characteristics of superconductor weak-link junctions*, Journal of Applied Physics **39**, 3113–3118 (1968)

[Min80] M. Minier and C. Minier: *Screening charge density around several* $\Delta Z = -1$ *impurities in copper: Nickel, palladium, platinum, and vacancy*, Physical Review B **22**, 21–27 (1980), DOI: 10.1103/PhysRevB.22.21

[Mur70] A. Murani: *Magnetic susceptibility and electrical resistivity of some gold-rare-earth alloys*, J.Phy.C. **2**, 153–158 (1970)

[Nyq28] H. Nyquist: *Thermal Agitation of Electric Charge in Conductors*, Physical Review **32**, 110–113 (1928), DOI: 10.1103/PhysRev.32.110

[Oli14] K. Olive *et al.* (Particle Data Group): *Review of Particle Physics*, Chin.Phys. **C38**, 090001 (2014), DOI: 10.1088/1674-1137/38/9/090001

[Pag10] G. Pagliaroli, F. Rossi-Torres and F. Vissani: *Neutrino mass bound in the standard scenario for supernova electronic antineutrino emission*, Astroparticle Physics **33**(5-6), 287–291 (2010), DOI: 10.1016/j.astropartphys.2010.02.007

[Per76] B. Perscheid, H. Büchsler and M. Forker: *Mössbauer study of the hyperfine interaction of ^{197}Au in gadolinium*, Physical Review B **14**, 4803–4807 (1976), DOI: 10.1103/PhysRevB.14.4803

[Pie12a] C. Pies: *maXs-200: Entwicklung und Charakterisierung eines Röntgendetektors basierend auf magnetischen Kalorimetern für die hochauflösende Spektroskopie hochgeladener Ionen*, Phd thesis, Heidelberg University (2012)

[Pie12b] C. Pies, S. Schäfer, S. Heuser *et al.*: *maXs: Microcalorimeter Arrays for High-Resolution X-Ray Spectroscopy at GSI/FAIR*, Journal of Low Temperature Physics **167**(3-4), 269–279 (2012), DOI: 10.1007/s10909-012-0557-z

[Pla13] Planck Collaboration: *Planck 2013 results. I. Overview of products and scientific results*, Astronomy & Astrophysics (2013), arXiv:1303.5076

[Ran14] P. C.-O. Ranitzsch: *Development and characterization of metallic magnetic calorimeters for the calorimetric measurement of the electron capture spectrum of ^{163}Ho for the purpose of neutrino mass determination*, Phd thesis, Heidelberg University (2014)

[Rei86] W. Reim, R. H. Koch, A. P. Malozemoff, M. B. Ketchen and H. Maletta: *Magnetic Equilibrium Noise in Spin-Glasses: $Eu_{0.4}Sr_{0.6}S$*, Physical Review Letters **57**, 905–908 (1986), DOI: 10.1103/PhysRevLett.57.905

[Rep12] J. Repp, C. Böhm, J. Crespo López-Urrutia *et al.*: *PENTATRAP: a novel cryogenic multi-Penning_trap experiment for high-precision mass measurements on highly charged ions*, Aplpied Physics B: Lasers and Optics **107**(4), 983–996 (2012), DOI: doi:10.1007/s00340-011-4823-6

[Rid65] P. Rider, K. Geschneider, Jr. and O. McMaster: *Gold-rich rare-earth-gold solid solutions*, Transactions of the Metallurgical Society of AIME **233**, 1488–1496 (1965)

[Rou12] C. Roux, C. Böhm, A. Dörr *et al.*: *The trap design of PENTATRAP*, Applied Physics B **107**(4), 997–1006 (2012)

[Sch00] J. Schönefeld: *Entwicklung eines mikrostrukturierten magnetischen Tieftemperatur-Kalorimeters zum hochauflösenden nachweis von einzelnen Röntgenqanten*, Phd thesis, Heidelberg University (2000)

[Seg09] F. V. Seggern: *Development of a metallic magnetic calorimeter towards a neutrino mass measurement*, Diploma thesis, Heidelberg University (2009)

[Sjø75] M. E. Sjøstrand and G. Seidel: *Hyperfine resonance properties of Er^{3+} in Au*, Physical Review B **11**, 3292–3297 (1975), DOI: 10.1103/PhysRevB.11.3292

[Ste51] K. Stevens: *Matrix Elements and Operator Equivalents Connected with the Magnetic Properties of Rare Earth Ions*, Proceedings physical society London **A65**, 209–215 (1951)

[Sve89] P. Svedlindh, K. Gunnarsson, P. Nordblad *et al.*: *Equilibrium magnetic fluctuations of a short-range Ising spin glass*, Physical Review B **40**, 7162–7166 (1989), DOI: 10.1103/PhysRevB.40.7162

[Tao71] L. J. Tao, D. Davidov, R. Orbach and E. P. Chock: *Hyperfine Splitting of Er and Yb Resonances in Au: A Separation between the Atomic and Covalent Contributions to the Exchange Integral*, Physical Review B **4**, 5–9 (1971), DOI: 10.1103/PhysRevB.4.5

[Van64] H. Van Kempen, A. Miedema and W. Huiskamp: *Heat capacities of the metals terbiumand holmium below 1K*, Physica **30**(1), 229–236 (1964)

[Wal77] L. R. Walker and R. E. Walstedt: *Computer Model of Metallic Spin-Glasses*, Physical Review Letters **38**, 514–518 (1977), DOI: 10.1103/PhysRevLett.38.514

[Wal80] L. R. Walker and R. E. Walstedt: *Computer model of metallic spin-glasses*, Physical Review B **22**, 3816–3842 (1980), DOI: 10.1103/PhysRevB.22.3816

[Wan12] M. Wang, G. Audi, A. Wapstra *et al.*: *The Ame2012 atomic mass evaluation*, Chinese Physics C **36**(12), 1603 (2012), DOI: 10.1088/1674-1137/36/12/003

[Weg13] M. Wegner: *Entwicklung eines 64-Pixel-Detektor-Arrays basierend auf mikrostrukturierten metallischen magnetischen Kalorimetern mit integriertem Mikrowellen-SQUID-Multiplexer*, Master thesis, Heidelberg University (2013)

[Wen99] K. Wendt, K. Blaum, B. Bushaw *et al.*: *Recent developments in and applications of resonance ionization mass spectrometry*, J. Anal. Chem. **364**, 471–477 (1999)

[Whi02] G. White and P. Meeson: *Experimental Techniques in Low-Temperature Physics, Monographs on the Physics and Chemistry of Materials*, Clarendon Press, Oxford (2002)

[Wil69] G. Williams and L. L. Hirst: *Crystal-Field Effects in Solid Solutions of Rare Earths in Noble Metals*, Physical Review **185**, 407–415 (1969), DOI: 10.1103/PhysRev.185.407

[Wiß13] V. Wissdorf: *Magnetisches 1/f-Rauschen und Imaginärteil der magnetischen Suszeptibilität von Erbium dotiertem Gold bei Millikelvin Temperaturen*, Bachelor thesis, Heidelberg University (2013)

Ich versichere, dass ich diese Arbeit selbständig verfasst und keine anderen als die angegeben Quellen und Hilfsmittel benutzt habe.

Heidelberg, den 01.06.2015 .....

(Sebastian Hähnle)